Cell Biol Toxicol (2022) 38:505–530
https://doi.org/10.1007/s10565-021-09624-x

ORIGINAL ARTICLE

Protecting mitochondria via inhibiting VDAC1 oligomerization alleviates ferroptosis in acetaminophen-induced acute liver injury

Baolin Niu · Xiaohong Lei · Qingling Xu · Yi Ju · Dongke Xu · Liya Mao · Jing Li · Yufan Zheng · Ning Sun · Xin Zhang · Yimin Mao · Xiaobo Li

Received: 8 March 2021 / Accepted: 10 June 2021 / Published online: 17 August 2021

Abstract Acetaminophen (APAP) overdose is a common cause of drug-induced liver injury (DILI). Ferroptosis has been recently implicated in APAP-induced liver injury (AILI). However, the functional role and underlying mechanisms of mitochondria in APAP-induced ferroptosis are unclear. In this study, the voltage-dependent anion channel (VDAC) oligomerization inhibitor VBIT-12 and ferroptosis inhibitors were injected via tail vein in APAP-injured mice. Targeted metabolomics and untargeted lipidomic analyses were utilized to explore underlying mechanisms of APAP-induced mitochondrial dysfunction and subsequent ferroptosis. As a result, APAP overdose led to characteristic changes generally observed in ferroptosis. The use of ferroptosis inhibitor ferrostatin-1 (or UAMC3203) and iron chelator deferoxamine further confirmed that ferroptosis was responsible for AILI. Mitochondrial dysfunction, which is associated with the tricarboxylic acid cycle and fatty acid β-oxidation suppression, may drive APAP-induced ferroptosis in hepatocytes. APAP overdose induced VDAC1 oligomerization in hepatocytes, and protecting mitochondria via VBIT-12 alleviated APAP-induced ferroptosis. Ceramide and cardiolipin levels were increased via

Baolin Niu, Xiaohong Lei and Qingling Xu contributed equally to this work.

Highlights
1. Ferroptosis is responsible for APAP-induced hepatocyte cell death.
2. Protecting mitochondria via inhibiting VDAC1 oligomerization attenuates APAP-induced ferroptosis.
3. *Taz* and *Smpd1*, responsible for CL and CER synthesis, affect APAP-induced mitochondrial dysfunction and subsequent ferroptosis in hepatocytes.
4. Levels of 4-HNE protein adducts are increased in the liver samples of patients with DILI.

B. Niu · Y. Ju · D. Xu · L. Mao · Y. Zheng · N. Sun · X. Li (✉)
Department of Physiology and Pathophysiology, School of Basic Medical Sciences, Fudan University, 130 Dong'an Rd, Shanghai 200032, China
e-mail: xbli@fudan.edu.cn

B. Niu
e-mail: niu_bl@126.com
Y. Ju
e-mail: yi_mailbox@163.com
D. Xu
e-mail: 17211010060@fudan.edu.cn
L. Mao
e-mail: 16301050265@fudan.edu.cn
Y. Zheng
e-mail: 17211010062@fudan.edu.cn
N. Sun
e-mail: sunning@fudan.edu.cn

UAMC3203 or VBIT-12 in APAP-induced ferroptosis in hepatocytes. Knockdown of *Smpd1* and *Taz* expression responsible for ceramide and cardiolipin synthesis, respectively, aggravated APAP-induced mitochondrial dysfunction and ferroptosis in hepatocytes, whereas *Taz* overexpression protected against these processes. By immunohistochemical staining, we found that levels of 4-hydroxynonenal (4-HNE) protein adducts were increased in the liver biopsy samples of patients with DILI compared to that in those of patients with autoimmune liver disease, chronic viral hepatitis B, and non-alcoholic fatty liver disease (NAFLD). In summary, protecting mitochondria via inhibiting VDAC1 oligomerization attenuated hepatocyte ferroptosis by restoring ceramide and cardiolipin content in AILI.

Keywords Acetaminophen-induced liver injury · Ferroptosis · 4-hydroxynonenal · Mitochondria · VDAC1

Abbreviations

APAP	Acetaminophen
DILI	Drug-induced liver injury
4-HNE	4-Hydroxynonenal
VDAC1	Voltage-dependent anion channel 1
AILI	APAP-induced liver injury
NAPQI	N-Acetyl-p-benzoquinone imine
GSH	Glutathione
ROS	Reactive oxygen species
AIH	Autoimmune liver disease
CHB	Chronic viral hepatitis B
NAFLD	Non-alcoholic fatty liver disease steatosis
ALD	Alcoholic liver disease
DFO	Deferoxamine
siRNA	Small interfering RNA
ALT	Alanine aminotransferase
AST	Aspartate aminotransferase
H&E	Hematoxylin and eosin
MMP	Mitochondrial membrane potential
MDA	Malondialdehyde
OCR	Oxygen consumption rate
MOM	Mitochondrial outer membrane
BSA	Bovine serum albumin
PA	Palmitic acid
LC-MS	Liquid chromatography-mass spectrometry
H-SCORE	Histological scores
ALP	Alkaline phosphatase
RNA-seq	RNA sequencing
GSEA	Gene set enrichment analysis
Fer-1	Ferrostatin-1
TUNEL	Terminal deoxynucleotidyl transferase-mediated dUTP nick-end labeling
PMHs	Primary mouse hepatocytes
DCFH-DA	Dichloro-dihydro-fluorescein diacetate
TCA	Tricarboxylic acid
ETC	Electron transport chain
CL	Cardiolipin
CER	Ceramide
Taz	Tafazzin

Introduction

Drug-induced liver injury (DILI) can lead to both clinically unexplained liver injury and liver failure (Andrade et al. 2019; Kullak-Ublick et al. 2017). Yearly incidence for DILI is 14–23.8/100,000 individuals (Bjornsson et al. 2013; Sgro et al. 2002; Shen et al. 2019). DILI diagnosis necessitates the ruling out of alternative, more prevalent conditions leading to such hepatic issues, together with the examination of specific drug treatment timeframes that could lead to drug-induced hepatic damage development,

X. Lei · J. Li · Y. Mao (✉)
Division of Gastroenterology and Hepatology, Key Laboratory of Gastroenterology and Hepatology, Ministry of Health, Renji Hospital, School of Medicine, Shanghai Institute of Digestive Disease, Shanghai Jiao Tong University, 145 mid-Shandong Rd, Shanghai 200001, China
e-mail: maoym11968@163.com

X. Lei
e-mail: m18224517701@163.com

Q. Xu
Department of Hepatology, Mengchao Hepatobiliary Hospital of Fujian Medical University, Fuzhou, Fujian, China

X. Zhang (✉)
Department of Pathology, Fudan University Zhongshan Hospital, 180 Fenglin Road, Shanghai 200032, China
e-mail: xzhangbwtx@163.com

combined with all follow-up clinical/pathology/laboratory features during follow-up (Hassan and Fontana 2019). The histopathological features of DILI include bile duct injury and lobular/portal hepatitis (Ettel et al. 2017; Lewis 2011). Although several high-potential genetic biomarkers for DILI have emerged (Church et al. 2019), there is still a lack of confirmatory, objective, and specific biomarkers.

Acetaminophen (N-acetyl-p-aminophenol, APAP) is a mainstay analgesic/antipyretic agent with an excellent therapeutic effect at recommended dosage regimens, though it can lead to hepatotoxicity if such dosage regimens are abused, rendering it a typical DILI-inducing drug. The most commonly used analgesic and antipyretic drug is safe and effective at therapeutic doses. APAP-induced liver injury (AILI) murine model perfectly reflects the features of acute DILI (Jaeschke et al. 2014). APAP-triggered cell death is initiated via cytochrome P450-derived N-acetyl-p-benzoquinone imine (NAPQI), which depletes liver glutathione (GSH) and ultimately forms adducts with cellular proteins. In hepatocytes, mitochondria are a main target for NAPQI protein adduct generation. Although radioactive APAP investigations highlighted that low levels of radioactive content covalent interplays took place within the mitochondrion (Jollow et al. 1973), changes to mitochondrial ultrastructure and functional deficits following APAP administration have been noted. In addition, the importance of mitochondrial free radicals, oxidative stress, and peroxynitrite formation on mediating APAP-induced injury has also been documented. Cytosolic proteins such as JNK/Bax undergo transport into the mitochondria, thereby amplifying oxidative stress, leading to the aperture of mitochondrion permeability transition pores (Ramachandran and Jaeschke 2019; Jaeschke 2018; Tujios and Fontana 2011).

Ferroptosis, a form of regulated cell death, occurs due to iron-dependent lipid peroxidation, being implicated in neurodegeneration, ischemia reperfusion, cancer, and other diseases. Under normal circumstances, system Xc^-/γ-GCS-GS/GPX4 protects cells against lipid peroxidation and inhibits ferroptosis. However, ferroptosis inducers suppress this axis, leading to lipid hydroperoxide accumulation through ACSL4/LPCAT3/LOX (Stockwell et al. 2017). Mitochondria are compromised during ferroptosis in different models, as evidenced by abnormal morphology, reactive oxygen species (ROS) bursts, alteration of membrane potential (MMP), exacerbated lipid peroxidation, and accumulation of iron within mitochondria (Wu et al. 2021; Bock and Tait 2020; Paul et al. 2017). However, no consensus has been reached on the functional orientation of mitochondria in ferroptosis (Wang et al. 2020).

In 2015, Lorincz et al. showed that ferroptosis was involved in APAP-induced cell death in primary hepatocytes (Lorincz et al. 2015). In 2020, Yamada et al. reported that ferroptosis driven by radical oxidation of n-6 polyunsaturated fatty acids mediated AILI (Yamada et al. 2020). As mitochondria play an important role in APAP-induced cell death, we can reasonably speculate their importance in APAP-induced ferroptosis; thus far, the role of mitochondria and its underlying mechanisms in APAP-induced ferroptosis have not yet been elucidated. To identify effective treatment options targeting mitochondria, the role of mitochondrial damage in APAP-induced ferroptosis requires in-depth investigation.

In the present study, the central role of ferroptosis in APAP-induced hepatotoxicity was further confirmed in mice and cultured hepatocytes. The voltage-dependent anion channel (VDAC) oligomerization inhibitor VBIT-12 was used to investigate the importance of mitochondria in APAP-induced ferroptosis. Targeted metabolomics and untargeted lipidomic analyses were utilized to explore underlying mechanisms of APAP-induced mitochondrial dysfunction and subsequent ferroptosis. We quantified 4-hydroxynonenal (4-HNE), one of the lipid peroxidation indicators, in liver biopsy samples of patients with DILI and other common liver diseases. The current study clarifies the mitochondrial mechanisms involved in AILI, which is characterized by ferroptosis-associated cell death, and identifies future avenues of research that may ultimately lead to effective treatments and management protocols to improve DILI patient outcomes.

Materials and methods

Animals and treatments

All in vivo experiments were accepted by the Animal Ethics Committee of Fudan University School of Basic Medical Sciences. Male C57 BL /6J mice (6–8 weeks; 18–22 g each) were procured from the Experimental Animal Centre of Shanghai SLAC. All mice were fed in laboratory in vivo facilities with ad libitum food and water, within a temperature-/humidity-regulated environment (22 ± 1 °C; Rh. = 65 ± 5%), adopting a 12-h circadian cycling process. Mice fasted overnight for

12 h and were randomly divided into different groups. An APAP [Sigma-Aldrich™, St Louis, MO, USA] solution (using 0.9% sodium chloride as solvent) was prepared immediately prior to trial commencement. UAMC3203 [MedChemExpress, USA, 10 mg/kg], deferoxamine [DFO, 100 mg/kg, Selleck Chemicals™, China], VBIT-12 [20 mg/kg; Selleck Chemicals ™, China], and dimethyl sulfoxide (DMSO) were administered via tail vein injection. The mice were treated with intraperitoneal administration of saline or 300 mg/kg APAP and then sacrificed to collect blood and liver after 6 h or 12 h.

Cell culture, small interfering RNA (siRNA) interference, and plasmid transfection

Primary hepatocytes were isolated from mice and purified through a collagenase IV perfusion protocol (Wang et al. 2017). Cells were liberated into Dulbecco's Modified Eagle's Medium (DMEM) after perfusion. A 45% Percoll gradient was used to separate live and dead hepatocytes. Cell cultures underwent twice washing events using DMEM followed by resuspension within the appropriate growth medium (DMEM, 10% fetal bovine serum [FBS]). Murine Hepa1-6 cell line was procured from the Cell Bank of Type Culture Collection of the Chinese Academy of Sciences (Shanghai, China) and grown using DMEM [Invitrogen™, Eugene, OR, USA] with 10% FBS, penicillin, streptomycin, and amphotericin B in a humidified incubator with 5% CO_2 at 37 °C.

Hepa1-6 cells were transfected using siRNA targeting murine *Taz* or *Smpd1* or control siRNAs, while *Taz* overexpression plasmid was transfected within Hepa1-6 cell cultures through Lipofectamine3000® [Life Technologies™, Thermo Fisher Scientific, USA] over a 48-h period, with subsequent APAP administration. The siRNA sequence against *Taz* was 5′-CCAG G A U U C A A G C A C A G C U T T / A G C UGUGCUUGAAUCCUGGTT-3′; the siRNA sequence against *Smpd1* was 5′-GGAG C C U C C C A G A U G C U A A T T / U U A G CAUCUGGGAGGCUCCTT-3′.

Biochemical/histopathology assays

Serum alanine transaminase (ALT) and aspartate transaminase (AST) activities were asserted through the appropriate analytical assay kits and conducted as described in the manufacturer's protocols [Nanjing Jiancheng Institute of Biotechnology, Nanjing, China]. For histological analyses, liver tissues from treated mice as indicated were fixated within 4% paraformaldehyde for one night, paraffin-coated, cut to produce 5-mm-thick slices, and finally underwent staining with hematoxylin/eosin (H&E).

Terminal dUTP nick-end labeling (TUNEL) stain protocol

DNA fragmentation was identified through TUNEL methodology, via in situ cell detection kit [Roche™, USA]. Tissue slice stains were conducted in line with manufacturer protocols. Consequently, cells having positively stained nuclei were identified by eye and underwent microscopy-based imaging [Leica DFC310 FX®; Leica™, Germany].

Immunohistochemical demonstration of 4-HNE-adducts

Sections were incubated with a rabbit anti-4-hydroxynonenal (4-HNE) antibody [#ab46545; Abcam™, Cambridge, UK] at 4 °C for one night, followed by incubation using horseradish peroxidase (HRP)-conjugated anti-rabbit antibody at room temperature for ninety minutes, visualization through DAB, and counterstaining using hematoxylin. The histological score (H-SCORE) was used to semi-quantify individual 4-HNE-stained samples.

Immunohistochemical results

The H-SCORE, calculated by multiplying the quantity and intensity scores, was used to semi-quantify 4-HNE staining for each tissue sample. The score setting parameters for quantity (degree of positively-stained cells) were as follows: score = 0, none; score = 1, 1–25%; score = 2, 26–50%; score = 3, 51–75%; and score = 4, 76–100%. Intensity scoring reflected the mean intensity of the positively stained cells, using a score range of: 0 (nil); 1 (low); 2 (intermediate); and 3 (high). Proportion/intensity scorings were consequently multiplied for obtaining a global score, having a range of 0 to 12. Individual samples were blind scrutinized by two experienced pathologists.

Celltiter-Glo® luminescent cell viability assay

Cell aliquots were seeded within opaque 96-well microplates with 1×10^4 cells/well. After attachment, cells were treated as indicated prior to undergoing CellTiter-Glo® Luminescent Cell Viability Assay [Promega™, Madison, WI, USA], according to the manufacturer's protocols. Luminous intensity from each well was registered through the BioTek™ SYNERGY H1 luminescence reading platform.

Lipid peroxides determination

In order to detect malondialdehyde (MDA) content in serum and understand the level of lipid peroxidation, MDA serum content was analyzed through the lipid peroxidation MDA assay kit [Beyotime™, Nanjing, China], in line with the manufacturer's protocols. The MDA level was registered using 532 nm through the appropriate microplate reading platform [BioTek SYNERGY H1].

To visualize the lipid peroxidation in cells, Hepa1-6 cellular aliquots were placed onto individual 35-mm petri dishes (3×10^5 cells/well) and grown for one night in complete medium. The cells treated as indicated were incubated with 2 μM BODIPY 581/591 C11 (Invitrogen) for 30 min, followed by triple washing step using phosphate-buffered saline (PBS). Fluorescence imaging was conducted through fluorescence microscopy, using Texas Red (590 nm, reduced dye) and FITC (510 nm, oxidized dye) as emission filters.

ROS/GSH/MMP analyses

Hepa1-6 cellular aliquots were seeded into 35-mm petri dishes (3×10^5 cells/well) and incubated (20 min) using 10 μM dichloro-dihydro-fluorescein diacetate (DCFH-DA) [Molecular Probe, Beyotime™, China] at 37 °C to identify any cellular ROS events, together with 5 μM MitoSox-Red [Molecular Probe, Invitrogen™] incubation (10 min) at 37 °C to identify any mitochondrion-based ROS events. All cell cultures were placed into incubation (30 min) using 20 μM cell-permeable fluorescent dye ThiolTracker™ Violet [Glutathione Detection Reagent, Invitrogen™] at 37 °C to identify cellular GSH expression. Cell cultures were also placed into incubation using JC-1 [5 mg/L, Beyotime™] for 20 min at 37 °C for mitochondrial membrane potential (MMP) determination. JC-1 infiltrates the functional mitochondrion, and at a reduced membrane potential, it exists as a green fluorescing monomer. The dyes were removed by PBS-based triple washing, and fluorescence was registered using the appropriate microscopy platform [Leica Dmi8®; Leica™, Germany].

Iron level determination

The content of non-heme iron in the serum of mice was determined using the serum iron determination assay [NJIBE, Nanjing, China]. Intracellular iron, cellular Fe^{2+}, and mitochondrial Fe^{2+} levels within Hepa1-6 cells were determined using calcein-acetoxymethyl ester (calcein-AM), FerroOrange, and Mito-FerroGreen [Dojindo™, Kumamoto, Japan], respectively. Calcein-AM has membrane permeability/fluorescing properties (through intracellular esterases). This molecule can be swiftly quenched through Fe^{2+} or Fe^{3+}, making it an excellent marker for labile iron pools. Quenching levels leads to accurate assessment for the quantitation of chelatable iron within cells. Hepa1-6 cells were seeded into 35-mm petri dishes (approx. 15,000) and treated as indicated. Cell cultures were placed into incubation using 2 μM calcein-AM, in PBS for 30 min at 37 °C. Changes in fluorescence intensity reflected the intracellular iron levels. Hepa1-6 cells, treated as indicated, were incubated with 1 μM FerroOrange or 5 μM Mito-FerroGreen for 30 min (37 °C). Dyes were removed by triple washing using PBS. Cellular fluorescence levels were observed using fluorescent microscopy [Leica Dmi8®; Leica™, Germany].

Transmission electron microscopy

The primary hepatocytes were treated as indicated, followed by a 2-h fixation period using 2.5% glutaraldehyde/phosphate buffer, followed by secondary fixation using 1% osmium tetroxide. After dehydration, embedding, and staining, images of the samples were acquired using a transmission electron microscope [JEOL™, Japan].

Targeted metabolomics profiling in Hepa1-6 cells

Hepa1-6 cells were pretreated with Fer-1 or DMSO for 2 h and then challenged with 20 mM APAP for another 6 h. Consequently, cell cultures were harvested/homogenized using 25 μL water and extracted with 185 μL cold acetonitrile/methanol (8/2, v/v). Following centrifugation, 30 μL supernatant was employed for derivatization with 20 μL derivatives using the Biomek

4000® platform [Beckman Coulter, Inc.™, Brea, CA, USA]. Following derivatization, evaporation, reconstitution, and centrifugation, 135 μL supernatant were transferred/mixed using internal standard reagents. An ultraperformance liquid chromatography/mass spectrometry (UPLC-MS/MS) platform [ACQUITY UPLC-Xevo TQ-S®; Waters Corp.™, Milford, MA, USA] was employed for quantifying all metabolites of interest within this investigation [Metabo-Profile Biotechnology Co., Ltd ™ Shanghai, China]. Platform optimizations were set as described below.

High-performance liquid chromatography (HPLC), column ACQUITY HPLC BEH C18 1.7 × 10^{-6} M VanGuard precolumn (2.1 × 5 mm)/ACQUITY HPLC BEH C18 1.7 × 10^{-6} M analytical column (2.1 × 100 mm), column temperature 40 °C; sample manager temperature 10 °C; mobile phase A = water with 0.1% formic acid; mobile phase B = acetonitrile/IPA (70:30); gradient conditions were 0–1 min (5% B), 1–11 min (5–78% B), 11–13.5 min (78–95% B), 13.5–14 min (95–100% B), 14–16 min (100% B), 16–16.1 min (100–5% B), 16.1–18 min (5% B); flow rate 0.40 mL min^{-1}; injection volume 5.0 μL.

Mass spectrometer, capillary 1.5 (ESI +), 2.0 (ESI-) Kv; source temperature 150 °C; de-solvation temperature 550 °C; and de-solvation gas flow 1000 L h^{-1}. A total of 310 standardized compounds (including 12 subclasses) were procured from Sigma-Aldrich™ [St. Louis, MO, USA] and Steraloids Inc.™ [Newport, RI, USA], together with TRC Chemicals™ [Toronto, ON, Canada]. Three separate class control compounds were typically implemented on this instrument. Raw datasets developed through UPLC-MS/MS were analyzed through QuanMET® [v2.0, Metabo-Profile™, Shanghai, China] for conducting peak integration, calibration, and quantification for individual metabolites.

Mitochondrial oxygen consumption rate (OCR) analysis

The OCR was determined through the XF96 Seahorse® extracellular flux analyzer [Seahorse Bioscience™, Billerica, MA, USA]. Freshly isolated primary murine hepatocytes or Hepa1-6 cell aliquots were implanted onto XF 96-well culture microplates to allow attachment overnight. Following attachment, the cells were pretreated with Fer-1 (1 μM), VBIT-12 (20 μM), or DMSO for 2 h and then challenged with APAP (20 mM) for another 6 h ($n = 6$). After treatment, culture media was exchanged with unbuffered, glucose-free DMEM (pH 7.4) supplemented using 10 mM pyruvate, followed by culturing in a CO_2-free incubator for 30 min. After measuring the initial OCR, respiratory inhibitors were loaded onto the analyzer through sequential oligomycin administrations (2 μM), FCCP (1μM), and rotenone (1 μM)/antimycin (1 μM). Baseline OCR was determined to be [$OCR_{initial} - OCR_{R+A}$]. Upper limit respiration rate was determined to be [$OCR_{FCCP} - OCR_{R+A}$].

Fatty acid β-oxidation

Hepa1-6 cells (10,000/well) were prepared within XF96 cell culture microplates. Twelve hours prior to assay, the medium was changed to substrate-limited growth media (XF base medium containing 500 μM glucose, 1 mM GlutaMAX, 500 μM carnitine, and 1% FBS) ($n = 6$). The cells were challenged with APAP (20 mM) for another 3 h. Consequently, attached cell cultures were rinsed using FAO assay medium (XF base medium containing 2 mM glucose, 500 μM carnitine, pH 7.4), followed by addition of 135 μL FAO assay medium/well and incubated for 30 min at 37 °C without CO_2. Just prior to assay commencement, 30 μL XF palmitate-bovine serum albumin FAO substrate (Palmitate:BSA), or bovine serum albumin (BSA), was introduced into relevant wells. Cells consequently underwent OCR measurement with subsequent common sequential injections of oligomycin (2 μM), FCCP (4 μM), and rotenone (1 μM)/antimycin (1 μM).

Lipidomic analyses

Murine liver (100 mg) was homogenized in 750 μL cold chloroform/methanol (2:1) solution using a high-throughput tissue grinder. The samples were placed on ice for 40 min, mixed with 0.19 mL water, and vortexed for 30 s, chilled on ice packs for 10 min, followed by centrifugation at 12000 rpm for 5 min at room temperature. A 300 μL aliquot from the lower layer was placed into another 2-mL centrifuging tube, followed by addition of 0.5 mL of chloroform/methanol (2:1) solution into the upper residue, vortexing for 30 s and centrifuging at 12000 rpm for 5 min at room temperature. A 400 μL aliquot from the lower layer was transferred and combined in a 2-mL centrifuge tube. The lipid extract was dried and re-dissolved in 200 μL isopropanol and vortexed for 30 s, followed by filtering across a 0.22-μm pore-sized membrane. A 20 μL aliquot

from all samples collected was taken and pooled to form the quality control (QC) samples. All remaining samples were employed for LC-MS lipidomic analysis.

Chromatographic segregation was accomplished using Thermo Ultimate 3000 system carrying the ACQUITY UPLC® BEH C18 [100 × 2.1 mm, 1.7 μm, Waters™] column, kept at 50 °C. Autosampler temperature was 8 °C. Analyte gradient elution was performed using acetonitrile:water = 60:40 (0.1% formic acid + 10 mM ammonium formate) (C) and isopropanol:acetonitrile = 90:10 (0.1% formic acid + 10 mM ammonium formate) (D) with a flow rate of 0.25 mL/min. 2 μL/sample was injected following equilibrium. An increasing linear gradient of solvent C (v/v) was employed accordingly: 0–5 min, 70–57% C; 5–5.1 min, 57–50% C; 5.1–14 min, 50–30% C; 14–14.1 min, 30% C; 14.1–21 min, 30–1% C; 21–24 min, 1% C; 24–24.1 min, 1–70% C; and 24.1–28 min, 70% C. All ESI-MSn assays were conducted through a Thermo Q Exactive Focus mass spectrometer, using a spray voltage of 3.5 kV and − 2.5 kV (positive/negative modes, respectively). Sheath and auxiliary gases were fixed at 30 and 10 arbitrary units, respectively. Capillary temperature was 325 °C. The Orbitrap analyzer scrutinized over a mass range of m/z 150–2000 for full scan, using a mass resolution of 35,000. Dat-dependent acquisition (DDA) MS/MS runs were conducted through HCD scan. Normalized collision energy was 30 eV. Dynamic exclusion was employed for excluding redundant datasets from MS/MS spectra. All raw data files were directly imported into LipidSearch software (version 4.0), allowing for the determination of retention time alignment, peak picking, deconvolution of adducts, relative abundance determination, and preliminary identification. An output data frame was developed that incorporated the list of time-aligned identified lipid characteristics (m/z; retention time) together with relative signal intensity (area of the chromatographic peak) for individual samples.

Quantitative real-time polymerase chain reaction (RT-qPCR) analysis

Total RNA was collected through TRIZOL® reagent [Life Technologies™, Thermo Fisher Scientific]. Consequently, cDNA synthesis was conducted through Prime Script RT® reagent kit [Takara™, Shiga, Japan]. Quantitative real-time PCR was conducted through SYBR Green PCR kit, with *36b4* and *Gapdh* being normalization/internal controls. All primers employed for such gene expression investigations are illustrated within Supplementary Table S1.

Western blotting

Cellular total protein was extracted through RIPA lysis buffer® [Beyotime™, Shanghai, China] together with phenylmethanesulfonyl fluoride (PMSF) and phosphatase inhibitor cocktail (PIC). Following protein quantification through BCA protein assay kit [Beyotime™, China], western blot analysis was conducted as described in the literature (Hong et al. 2019). β-actin served as loading control. Samples (30 μg) were diluted in sample buffer and subjected to sodium dodecyl sulfate-polyacrylamide gel electrophoresis (SDS-PAGE). Primary antibodies employed were murine anti-rat/murine OXPHOS Cocktail (Invitrogen™ #458099, 1:5,000), rabbit anti-rat/murine PHB2 (CST™ #14085, 1:1,000), rabbit anti-rat/murine TAZ (Affinity™ #DF4653, 1:1,000), and rabbit anti-rat/murine SMPD1 (Affinity™ #DF4653, 1:1,000) and rabbit anti-rat/murine CYP2E1 (Proteintech™ #19937-1-AP, 1:2,000). The proteomic bands were visually identified through by enhanced chemiluminescence [ECL, Amersham Biosciences™, USA], with membranes being consequently developed and analyzed quantitatively through the appropriate imaging system [Tanon™, China].

VDAC1 cross-linking assay

In order to determine varying VDAC1 oligomers, cellular chemical cross-linking was performed as described previously, using a membrane permeable cross-linker, ethylene glycolbis (succinimide succinate) (EGS) (Nagakannan et al. 2019). Briefly, primary murine hepatocytes are treated as indicated, twice-washed through PBS, harvested by scraping, and placed into incubation using 0.5 mM EGS in PBS (pH 7.4) at room temperature for 30 min. In order to quench additional levels of cross-linker, 1.5 M Tris HCl (pH 7.8) was introduced (20 mM final conc.) and placed into incubation for 5 min at room temperature. Such a resulting mixture underwent centrifugation (10,000×*g* for 5 min), with resulting pellet undergoing lysis within iced NP-40 lysis buffer. Samples (50 μg) were diluted within relevant buffer (no β-mercaptoethanol) and underwent SDS-PAGE/immunoblotting through anti-VDAC1 antibody [#sc-390996, Santa Cruz Biotechnology™, USA].

Collection of biopsy samples from patients

Specimens consisted of 34 needle biopsies taken from patients with DILI (18 men, 16 women; age range: 23–

69 years). DILI was diagnosed based on criteria of the international consensus meetings (international classification) (European Association for the Study of the Liver. Electronic address eee, Clinical Practice Guideline Panel C, Panel m, representative EGB 2019; Yu et al. 2017). Controls involved the examination of needle biopsy specimens from 15 autoimmune liver disease (AIH), 14 chronic viral hepatitis B (CHB), and 14 non-alcoholic fatty liver disease steatosis (NAFLD), together with 5 alcoholic liver disease (ALD) patients. The clinical data of patients with DILI are shown in Supplementary Table S2, numbered from patient 1–34. Informed consent was collected for all investigation participants. This investigation was accepted by the Ethics Committee of Shanghai Jiaotong University Renji Hospital according to ethical guidelines of the 1975 Declaration of Helsinki.

Statistical analyses

Datasets were presented as means ± standard error of mean (SEM). Statistical analyses were performed through GraphPad Prism 8.0® Software [Prism Software™, San Diego, CA, USA]. Comparative analyses using two parameters were performed through two-tailed Student's *t* test. Multi-parameter analyses were performed through one-way analysis of variance (ANOVA) with subsequent recommended post-hoc analyses in GraphPad Prism 8.0 Software. For in vitro studies, mean and SEM values were asserted through 3–4 biological replicates from each representative trial. Trials were carried out in triplicate, on separate occasions. $P < 0.05$ was deemed to confer statistical significance.

Drawings

The graphical abstract was created with BioRender (https://biorender.com).

Results

Ferroptosis is responsible for APAP-induced hepatocyte cell death in vivo

To determine the possible role of ferroptosis in AILI, we reanalyzed our published RNA sequencing (RNA-seq) data from mice liver samples injected with saline or APAP (300 mg/kg and 750 mg/kg) for 3 or 6 h (Li et al. 2018). The raw RNA-seq data were deposited at SRA database of NCBI with the accession number PRJNA731100. We created a ferroptosis gene set based on ferroptosis pathways annotated in the Kyoto Encyclopedia of Genes and Genomes (KEGG) database, and these genes are shown in a heatmap (Fig. 1a). Transcriptomes of the 300 mg/kg APAP and saline group and the 750 mg/kg APAP and saline group at 3 h and 6 h were compared using gene set enrichment analysis (GSEA). The normalized enrichment scores (NESs) and enrichment significance for the ferroptosis gene set were also plotted. GSEA showed that ferroptosis was significantly upregulated in the AILI group (Fig. 1a). Expression of genes involved in ferroptosis, including ACSL4, GPX4, and HMOX1, significantly changed in APAP-injured mice, compared with those of mice in the control group (Fig. 1a). Next, we pretreated or treated APAP-injured mice with the ferroptosis-specific inhibitor UAMC3203 (derived from Fer-1 for improved in vivo efficacy) (Devisscher et al. 2018) or the iron chelator deferoxamine (DFO) via tail vein injection. Mice pretreated with UAMC3203 (10 mg/kg) at 30 min prior to APAP injection showed a drastic reduction in ALT and AST levels upon APAP

Fig. 1 Ferroptosis is responsible for APAP-induced hepatocyte cell death in vivo. Mice were pretreated/treated with UAMC3203 (10 mg/kg), DFO (100 mg/kg), or vehicle via tail vein injection for 30 min before APAP (300 mg/kg) injection. After 10 h, serum and liver samples were collected. a GSEA plots of liver transcriptomes from mice injected with saline or different doses of APAP (300 mg/kg and 750 mg/kg) for 3 or 6 h showed ferroptosis upregulation. Heatmaps show the relative expression of genes involved in ferroptosis ($n = 3$). b Serum ALT and AST levels in vehicle- or UAMC3203-pretreated AILI mice were measured ($n = 5$ mice/group, *t* test). c Serum MDA levels in vehicle- or UAMC3203-pretreated AILI mice were measured ($n = 5$ mice/group, *t* test). d Liver sections obtained from vehicle- or UAMC3203-pretreated AILI mice were stained with H&E, TUNEL, and 4-HNE immunohistochemical stains; scale bars represent 100 μm. Black arrows indicate positive staining. e Western blot analysis of CYP2E1 protein levels in vehicle- or UAMC3203-pretreated AILI mice ($n = 5$ mice/group, *t* test). f Serum ALT and AST levels in vehicle- or DFO-pretreated AILI mice were measured ($n = 5$ mice/group, *t* test). g Serum non-heme iron levels in vehicle- or DFO-pretreated AILI mice were measured ($n = 5$ mice/group, *t* test). h Liver sections obtained from vehicle- or DFO-pretreated AILI mice were stained with H&E, TUNEL, and 4-HNE immunohistochemical stains; scale bars represent 100 μm. Black arrows indicate positive staining. i Western blot analysis of CYP2E1 protein levels in vehicle- or DFO-pretreated AILI mice ($n = 5$ mice/group, *t* test)

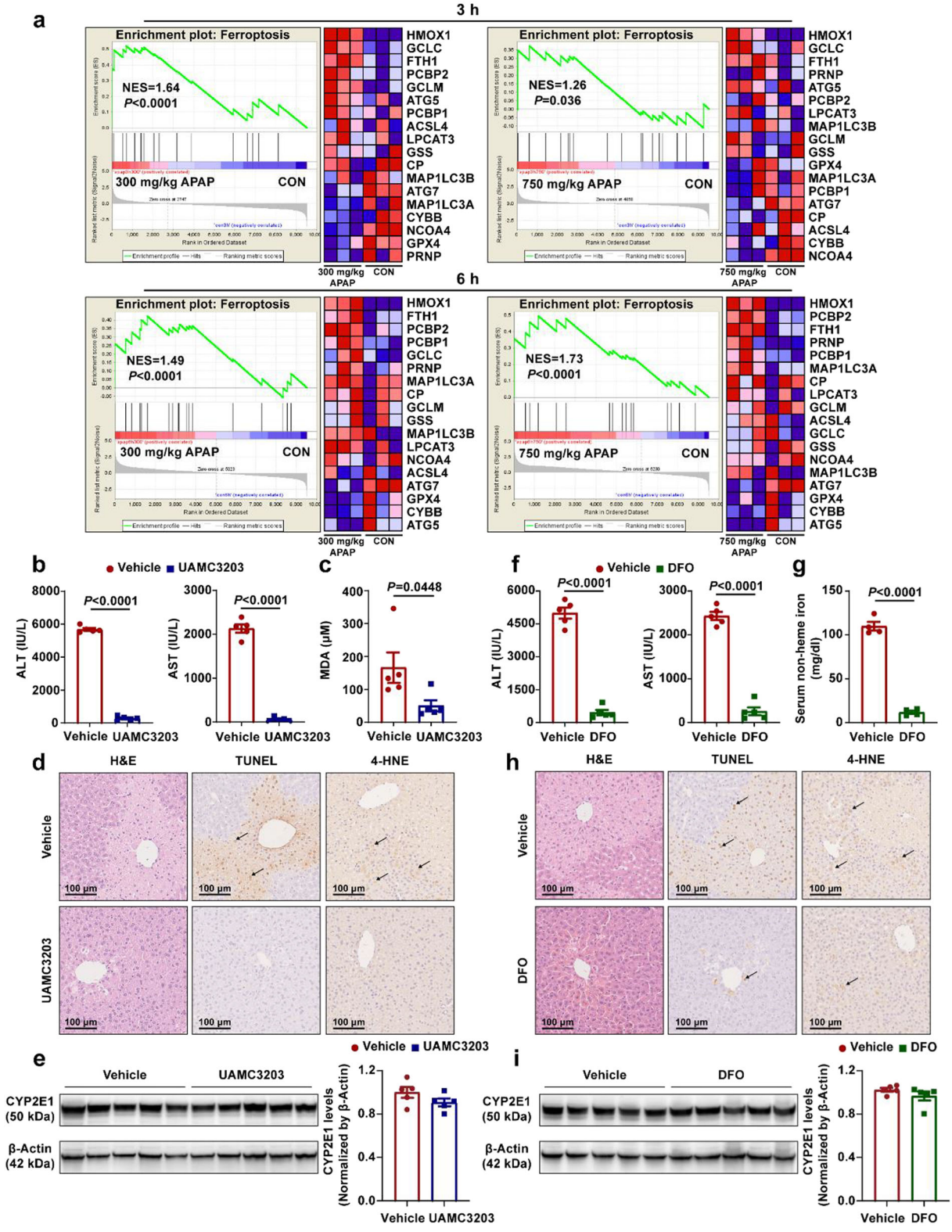
a
3 h
Enrichment plot: Ferroptosis
NES=1.64
P<0.0001
300 mg/kg APAP
CON
HMOX1
GCLC
FTH1
PCBP2
GCLM
ATG5
PCBP1
ACSL4
LPCAT3
GSS
CP
MAP1LC3B
ATG7
MAP1LC3A
CYBB
NCOA4
GPX4
PRNP
300 mg/kg APAP
CON
Enrichment plot: Ferroptosis
NES=1.26
P=0.036
750 mg/kg APAP
CON
HMOX1
GCLC
FTH1
PRNP
ATG5
PCBP2
LPCAT3
MAP1LC3B
GCLM
GSS
GPX4
MAP1LC3A
PCBP1
ATG7
CP
ACSL4
CYBB
NCOA4
750 mg/kg APAP
CON
6 h
Enrichment plot: Ferroptosis
NES=1.49
P<0.0001
300 mg/kg APAP
CON
HMOX1
FTH1
PCBP2
PCBP1
GCLC
PRNP
MAP1LC3A
CP
GCLM
GSS
MAP1LC3B
LPCAT3
NCOA4
ACSL4
ATG7
GPX4
CYBB
ATG5
300 mg/kg APAP
CON
Enrichment plot: Ferroptosis
NES=1.73
P<0.0001
750 mg/kg APAP
CON
HMOX1
PCBP2
FTH1
PRNP
PCBP1
MAP1LC3A
CP
LPCAT3
GCLM
ACSL4
GCLC
GSS
NCOA4
MAP1LC3B
ATG7
GPX4
CYBB
ATG5
750 mg/kg APAP
CON
b
Vehicle
UAMC3203
ALT (IU/L)
P<0.0001
Vehicle UAMC3203
AST (IU/L)
P<0.0001
Vehicle UAMC3203
c
MDA (μM)
P=0.0448
Vehicle UAMC3203
f
Vehicle
DFO
ALT (IU/L)
P<0.0001
Vehicle DFO
AST (IU/L)
P<0.0001
Vehicle DFO
g
Serum non-heme iron (mg/dl)
P<0.0001
Vehicle DFO
d
H&E
TUNEL
4-HNE
Vehicle
UAMC3203
100 μm
h
H&E
TUNEL
4-HNE
Vehicle
DFO
100 μm
e
Vehicle
UAMC3203
CYP2E1 (50 kDa)
β-Actin (42 kDa)
CYP2E1 levels (Normalized by β-Actin)
Vehicle UAMC3203
i
Vehicle
DFO
CYP2E1 (50 kDa)
β-Actin (42 kDa)
CYP2E1 levels (Normalized by β-Actin)
Vehicle DFO

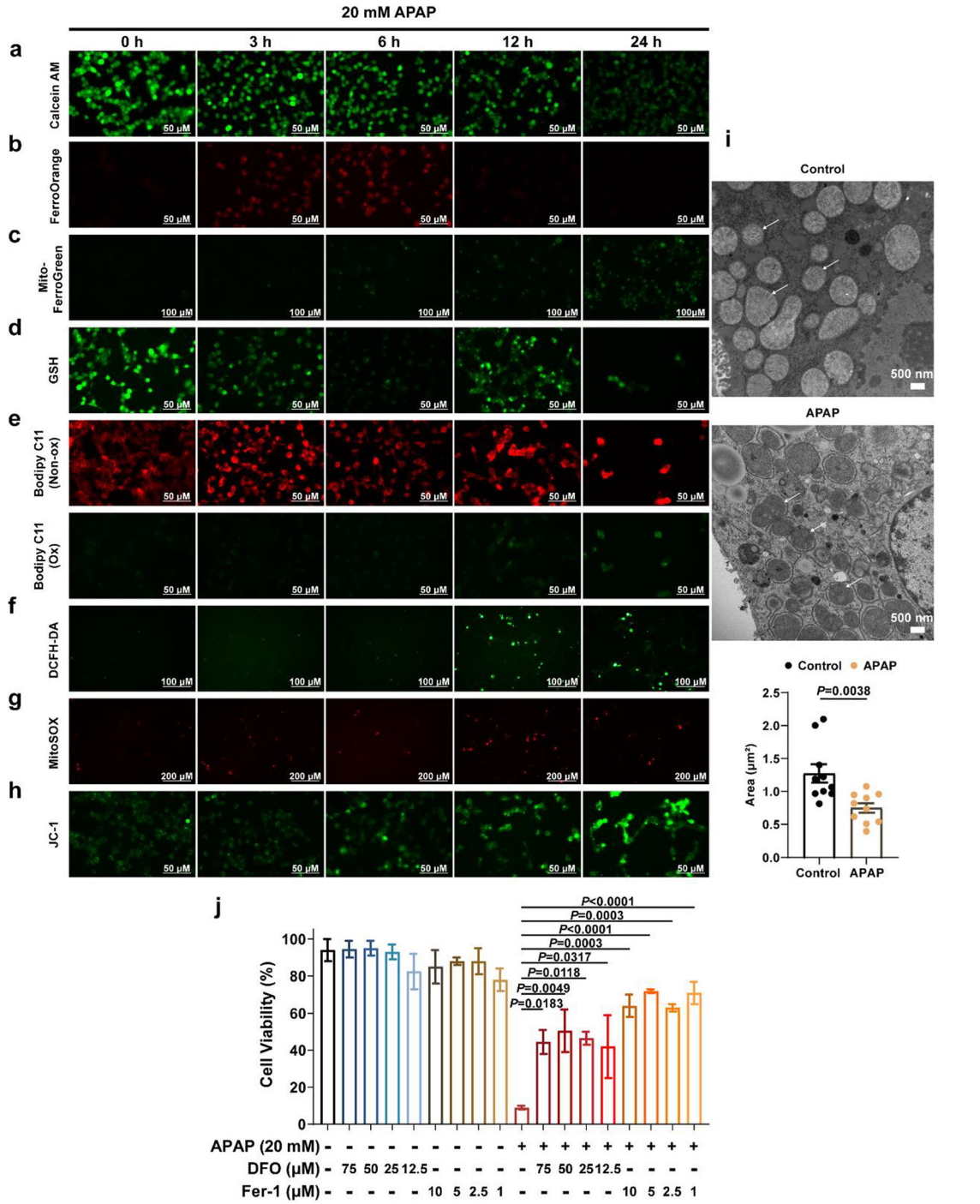

Fig. 2 Ferroptosis is responsible for APAP-induced hepatocyte cell death in vitro. **a**–**h** Representative images of (**a**) calcein-AM, (**b**) FerroOrange, (**c**) Mito-FerroGreen, (**d**) GSH, (**e**) Bodipy 581/591 C11, (**f**) DCFH-DA, **g** MitoSOX, and (**h**) JC-1 fluorescence in Hepa1-6 cells treated with 20 mM APAP for 0, 3, 6, 12, and 24 h. **i** Representative transmission electron microscopic images of the mitochondrial structure and corresponding relative mitochondrial area statistics in control and APAP-injured PMHs (*t* test). White arrows indicate the mitochondrial structure. **j** PMHs were pretreated with different concentrations of Fer-1 and DFO for 2 h and then challenged with 20 mM APAP for 12 h. Cell viability was determined using a CellTiter-Glo® luminescent cell viability assay (one-way ANOVA)

challenge, compared with that of the control group (Fig. 1b). These mice also showed reduced levels of the lipid peroxidation product MDA in liver tissue (Fig. 1c) and decreased injured area and number of TUNEL-positive stained and 4-HNE protein adduct-positive stained cells in liver histological sections (Fig. 1d). In order to rule out the possibility of Fer-1 affecting APAP metabolism, we evaluated the expression of CYP2E1, a key enzyme in APAP metabolism, and showed that UAMC3203 had no effect on CYP2E1 protein level in the liver (Fig. 1e). Moreover, mice pretreated with DFO (100 mg/kg) at 30 min prior to APAP injection showed decreases in ALT, AST (Fig. 1f), and serum non-heme iron contents (Fig. 1g), as well as improvements in liver pathology (Fig. 1h). DFO also had no effect on CYP2E1 protein level in the liver (Fig. 1i). Similarly, mice treated with UAMC3203 (Supplementary Fig. 1a) or DFO (Supplementary Fig. 1b) at 15 min after APAP injection showed decreased serum ALT/AST levels and also improved liver damage upon APAP challenge compared with that of the control group. Taken together, ferroptosis was responsible for the hepatotoxicity in APAP-injured mice.

Ferroptosis is responsible for APAP-induced hepatocyte cell death in vitro

To further study the possible role of ferroptosis in APAP-induced hepatotoxicity, we used Hepa1-6 cells and primary mouse hepatocytes (PMHs) to examine the direct effect of APAP challenge in vitro. A calcein-AM probe was used to assay the intracellular labile iron. The amount of chelatable iron was estimated via the degree of calcein quenching (Fig. 2a, Supplementary Fig. 2a). FerroOrange (Fig. 2b, Supplementary Fig. 2b) and Mito-FerroGreen (Fig. 2c, Supplementary Fig. 2c) were used for intracellular Fe^{2+} and mitochondrial Fe^{2+} detection, respectively. A GSH probe (ThiolTracker™ Violet) (Fig. 2d, Supplementary Fig. 2d), BODIPY 581/591 C11 (BODIPY) (Fig. 2e, Supplementary Fig. 2e), DCFH-DA (Fig. 2f, Supplementary Fig. 2f), MitoSOX (Fig. 2g, Supplementary Fig. 2g), and JC-1 (Fig. 2h, Supplementary Fig. 2h) were used to detect the levels of GSH, lipid peroxidation, oxidative species, mitochondrial ROS, and MMP, respectively. As a result, intracellular iron, especially mitochondrial iron, was considerably overloaded; lipid peroxides and intracellular and mitochondrial ROS were accumulated; and GSH was depleted following APAP challenge. JC-1 staining demonstrated that the MMP decreased with APAP overdose. APAP-injured PMHs exhibited the characteristic morphological features of ferroptosis (Wang et al. 2020), including a reduction in mitochondrial membrane density and corresponding volume (Fig. 2i), diminished or vanished mitochondrial crista, and a rupturing of the outer membrane. Fer-1 and DFO significantly increased PMH viability during a 20 mM APAP challenge (Fig. 2j). Taken together, ferroptosis was responsible for APAP-induced hepatotoxicity in vitro.

Levels of TCA cycle metabolites are enhanced by Fer-1 in APAP-injured hepatocytes

To investigate the underlying mechanisms of APAP-induced ferroptosis, we performed targeted metabolomics analysis using mouse Hepa1-6 cells treated with ferroptosis inhibitor Fer-1 in the presence and absence of 20 mM APAP for 6 h. Among the 310 metabolites with standard substances, 175 metabolites, including amino acids, fatty acids, carbohydrates, organic acids, carnitine, and other metabolites, were present in Hepa1-6 cells (Supplementary Fig. 3a, Fig.3a). Following Fer-1 treatment, TCA-related organic acids (Fer-1+APAP/Fer-1 vs. APAP/DMSO) were the most significantly upregulated metabolites (Fig. 3b); specifically, citric acid and aconitic acid levels increased by up to 16-fold and 11-fold, respectively. Levels of metabolites involved in the TCA cycle, including citric acid, aconitic acid, fumaric acid, and maleic acid, significantly increased following APAP challenge in the Fer-1-treated group, but not in the DMSO-treated group (Fig. 3c–f). As shown in Fig. 3g and 3h, APAP overdose led to decreased basal and maximal OCRs and reduced the capacity of fatty acid oxidation in Hepa1-6 cells.

Taken together, levels of TCA cycle metabolites were increased by Fer-1 in APAP-injured hepatocytes. These findings indicate that impaired energy generation caused by mitochondrial dysfunction, as associated with TCA cycle and fatty acid β-oxidation suppression, may drive APAP overdose-induced ferroptosis.

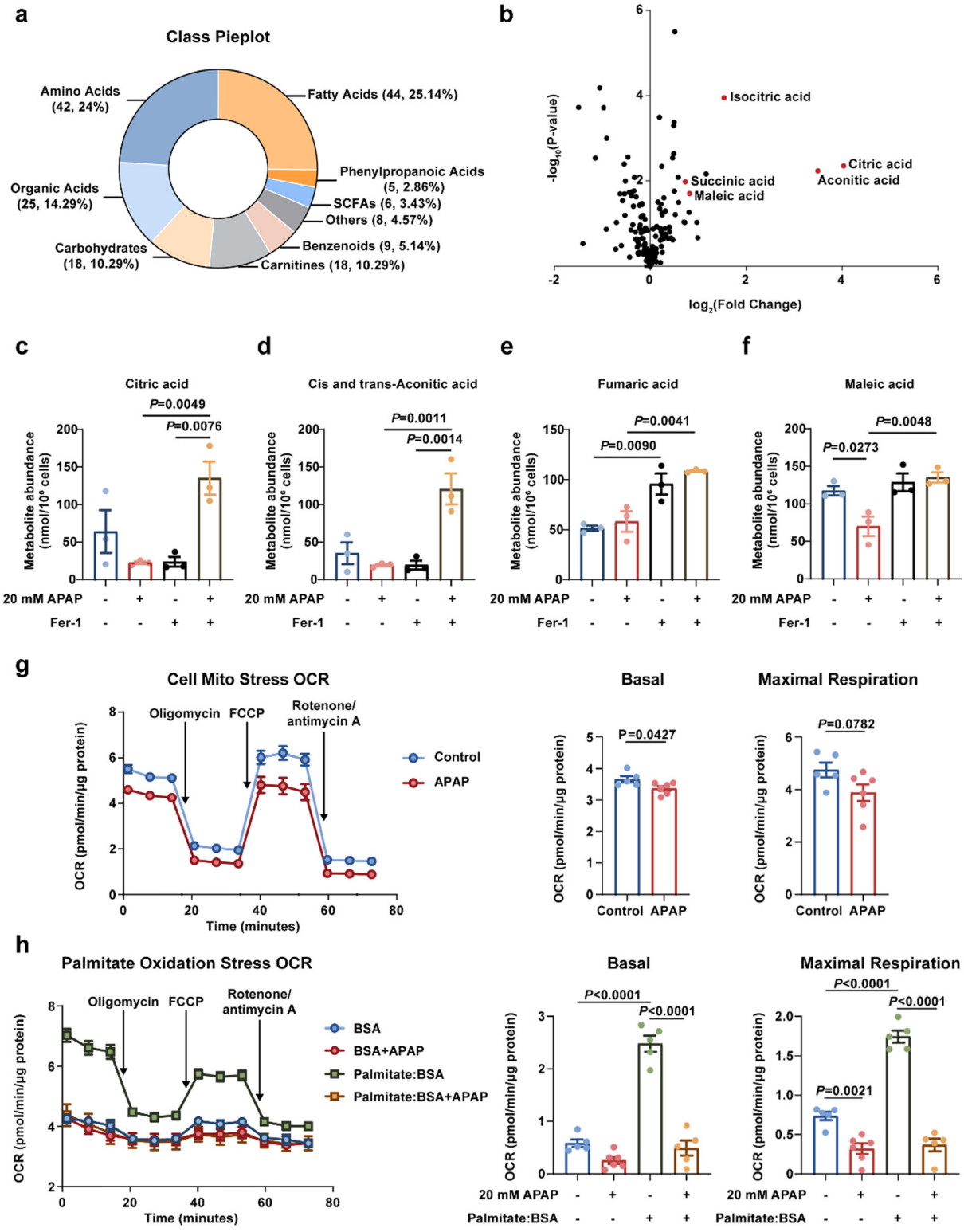
a
Class Pieplot
Amino Acids (42, 24%)
Fatty Acids (44, 25.14%)
Phenylpropanoic Acids (5, 2.86%)
SCFAs (6, 3.43%)
Others (8, 4.57%)
Benzenoids (9, 5.14%)
Carnitines (18, 10.29%)
Carbohydrates (18, 10.29%)
Organic Acids (25, 14.29%)
b
-log10(P-value)
log2(Fold Change)
Isocitric acid
Citric acid
Aconitic acid
Succinic acid
Maleic acid
c
Citric acid
d
Cis and trans-Aconitic acid
e
Fumaric acid
f
Maleic acid
Metabolite abundance (nmol/10⁶ cells)
20 mM APAP
Fer-1
g
Cell Mito Stress OCR
Oligomycin
FCCP
Rotenone/ antimycin A
Control
APAP
OCR (pmol/min/μg protein)
Time (minutes)
Basal
Maximal Respiration
h
Palmitate Oxidation Stress OCR
BSA
BSA+APAP
Palmitate:BSA
Palmitate:BSA+APAP

Fig. 3 Levels of TCA cycle metabolites are enhanced by Fer-1 in APAP-injured hepatocytes. **a** Pie chart of the average abundance composition ratio of various metabolites detected in the samples. **b** Volcano plot of metabolomics data from vehicle- and Fer-1-pretreated APAP groups (Fer-1+APAP/Fer-1 vs. APAP/DMSO) (n = 3/group). **c–f** Top 4 altered TCA-related organic acids identified via targeted metabolomics analysis, including (**c**) citric acid, (**d**) aconitic acid, (**e**) fumaric acid, and **f** maleic acid (n = 3/group, one-way ANOVA). **g** Cell mito stress OCRs were measured using Seahorse XF analysis with the indicated reagents in Hepa1-6 cells challenged with 20 mM APAP for 6 h. Arrows indicate the time when oligomycin, FCCP, and antimycin/rotenone were added to cells (n = 5–6/group, one-way ANOVA). **h** Palmitate oxidation stress OCRs were measured using Seahorse XF analysis with the indicated reagents in control and APAP-injured Hepa1-6 cells. Arrows indicate the time when oligomycin, FCCP, and antimycin/rotenone were added to cells (n = 5–6/group, one-way ANOVA). BSA was used as a control for palmitate:BSA

Protecting mitochondria using VBIT-12, a VDAC1 oligomerization inhibitor, attenuates APAP-induced ferroptosis

VDAC1 controls the transport of metabolites and ions between the mitochondria and cytoplasm, also controlling ROS production. Under the stimulation of apoptotic factors, VDACs assemble into oligomers including dimers, trimers, and tetramers, forming large holes in the mitochondrial outer membrane (MOM) and increasing MMP (Kim et al. 2019). The ability of APAP to induce VDAC oligomerization in PMHs was examined using ethylene glycol bis (succinimidyl succinate)-based cross-linking and immunoblotting with anti-VDAC antibodies. As a result, VDAC1 oligomer levels increased significantly in a time-dependent manner following APAP challenge (Fig. 4a). To investigate the possible role of mitochondrial dysfunction in APAP-induced ferroptosis, we used VBIT-12 (Kim et al. 2019; Shoshan-Barmatz et al. 2018; Ben-Hail et al. 2016), a VDAC1 oligomerization inhibitor, to treat APAP overdose-induced hepatotoxicity. VBIT-12 suppressed VDAC1 oligomerization in PMHs (Fig. 4b). As shown in Fig. 4c, VBIT-12- or Fer-1-pretreated PMHs show markedly increased viability following APAP challenge. Furthermore, increases in both intracellular and mitochondrial iron and ROS and lipid peroxide levels, as well as decreases in APAP overdose-induced MMP levels, were dramatically attenuated by VBIT-12 or Fer-1 in Hepa1-6 cells (Fig. 4d). In PMHs, APAP challenge resulted in decreased basal and maximal mitochondrial OCRs, each of which was significantly attenuated via VBIT-12 or Fer-1 pretreatment (Fig. 4e).

Taken together, VDAC1 oligomerization inhibitor protected mitochondria from APAP overdose-induced VDAC1 oligomerization in hepatocytes. Furthermore, Fer-1 alleviated APAP-induced ferroptosis in vitro.

VBIT-12 protects mice against AILI and ferroptosis

As VBIT-12 exerted a protective effect on hepatocytes, we examined its protective effect on AILI in vivo. In response to APAP challenge, serum ALT and AST levels drastically decreased following VBIT-12 pretreatment (Fig. 5a). Histological observation of the liver demonstrated alleviated damage in VBIT-12-pretreated AILI mice, compared with that in the APAP-challenged mice (Fig. 5b, c). TUNEL staining showed that DNA fragmentation was attenuated by VBIT-12 in the mouse liver (Fig. 5b, c). Moreover, 4-HNE staining revealed that lipid peroxidation markedly decreased following VBIT-12 pretreatment (Fig. 5b, c). We detected CYP2E1 protein level in the liver of mice treated with VBIT-12 and ruled out the effect of VBIT-12 on APAP metabolism. The results showed that the expression of CYP2E1 protein was not affected by VBIT-12 in the liver (Fig. 5d). Meanwhile, protein levels of mitochondrial ETC complexes I, II, III, and IV in the liver tissue of APAP-injured mice markedly increased following VBIT-12 pretreatment (Fig. 5e, Supplementary Fig.4a, b). Taken together, VBIT-12 protected mice against AILI and ferroptosis.

Ceramide (CER) and cardiolipin (CL) levels are increased by UAMC3203 and VBIT-12

To further elucidate the effects of ferroptosis inhibitor UAMC3203 and VDAC1 oligomerization inhibitor VBIT-12 on AILI, we collected liver samples from mice treated with vehicle (control) or APAP in the absence or presence of UAMC3203 or VBIT-12 pretreatment. Next, we performed LC-MS-based untargeted lipidomics analyses to identify changes in lipid composition. Partial least squares-discriminant

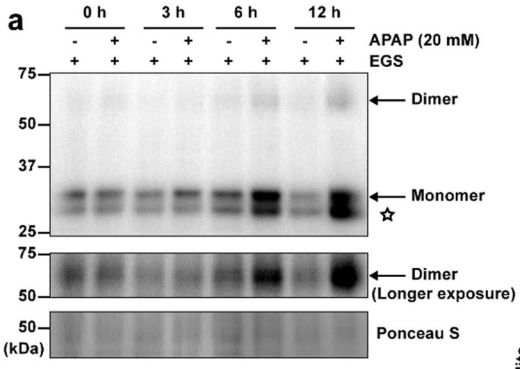
a
0 h
3 h
6 h
12 h
APAP (20 mM)
EGS
75
50
37
25
Dimer
Monomer
Dimer
(Longer exposure)
50
(kDa)
Ponceau S

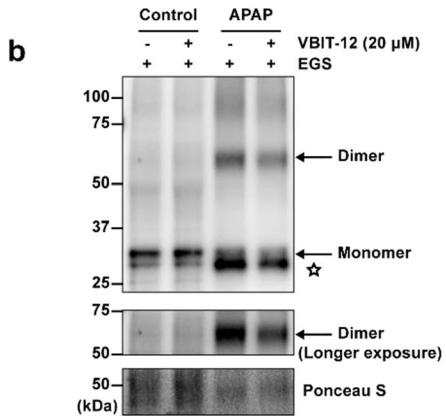
b
Control
APAP
VBIT-12 (20 μM)
EGS
100
75
50
37
25
Dimer
Monomer
Dimer
(Longer exposure)
50
(kDa)
Ponceau S

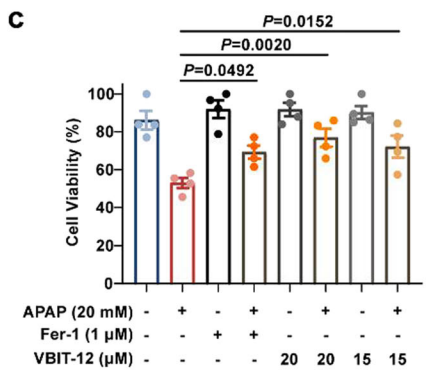
c
P=0.0152
P=0.0020
P=0.0492
Cell Viability (%)
100
80
60
40
20
0
APAP (20 mM)
Fer-1 (1 μM)
VBIT-12 (μM)
20
20
15
15

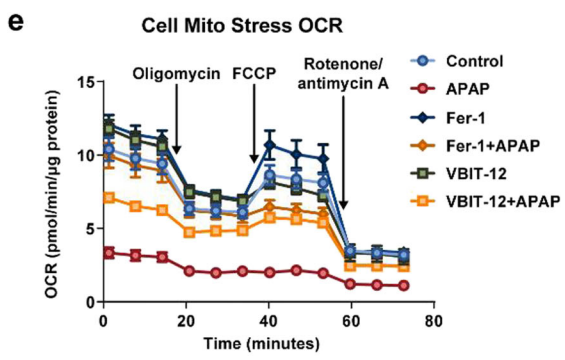
e
Cell Mito Stress OCR
Oligomycin
FCCP
Rotenone/
antimycin A
OCR (pmol/min/μg protein)
Time (minutes)
Control
APAP
Fer-1
Fer-1+APAP
VBIT-12
VBIT-12+APAP

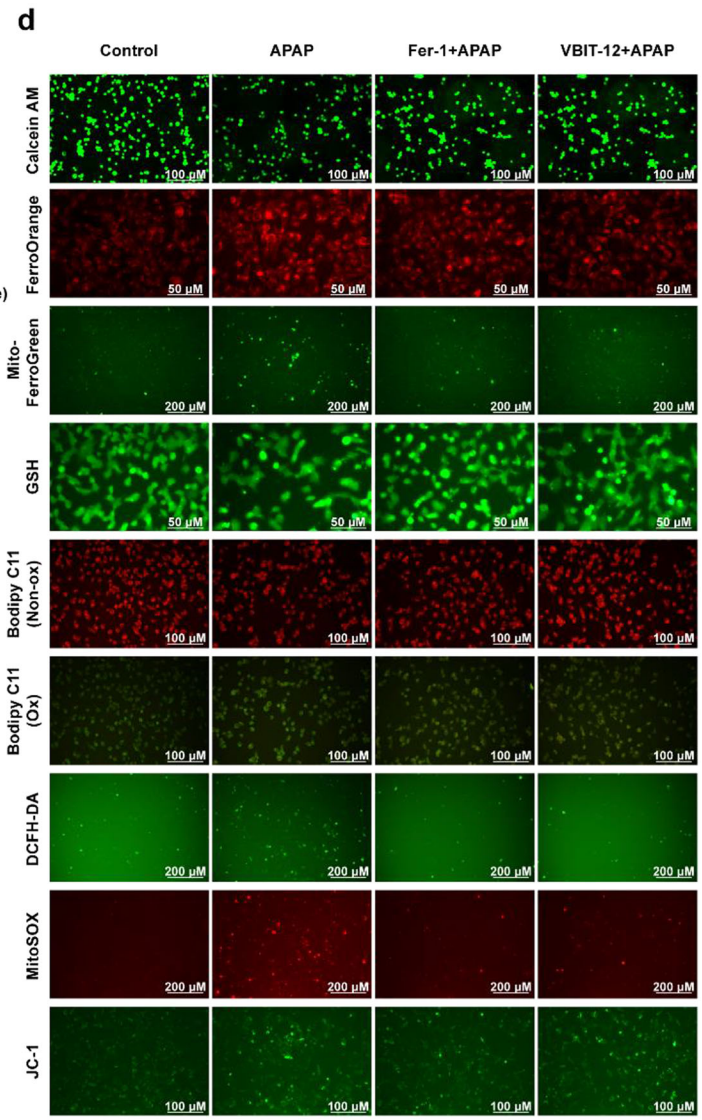
d
Control
APAP
Fer-1+APAP
VBIT-12+APAP
Calcein AM
FerroOrange
Mito-FerroGreen
GSH
Bodipy C11 (Non-ox)
Bodipy C11 (Ox)
DCFH-DA
MitoSOX
JC-1
100 μM
50 μM
200 μM

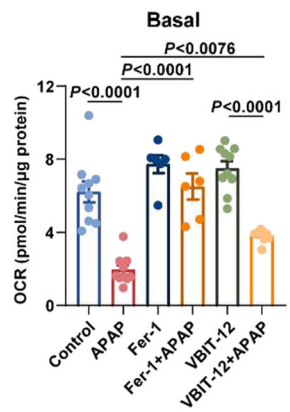
Basal
P<0.0076
P<0.0001
P<0.0001
P<0.0001
OCR (pmol/min/μg protein)
Control
APAP
Fer-1
Fer-1+APAP
VBIT-12
VBIT-12+APAP

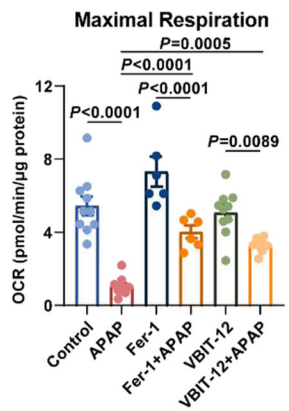
Maximal Respiration
P=0.0005
P<0.0001
P<0.0001
P<0.0001
P=0.0089
OCR (pmol/min/μg protein)
Control
APAP
Fer-1
Fer-1+APAP
VBIT-12
VBIT-12+APAP

Fig. 4 Protecting mitochondria using VBIT-12, a VDAC1 oligomerization inhibitor, attenuates APAP-induced ferroptosis. **a** Primary mouse hepatocytes were challenged with 20 mM APAP for the indicated time periods. Next, cells were harvested and incubated in the presence of ethylene glycol bis (succinimidyl succinate) to cross-link proteins and then subjected to western blotting to assess the oligomeric status of VDAC1. Arrows indicate the monomer and dimer forms of VDAC1. Asterisk (*) indicates the intramolecular cross-linked bands. **b** PMHs pretreated with VBIT-12 (20 μM) for 2 h were challenged with 20 mM APAP for 12 h. Next, cells were harvested and incubated in the presence of ethylene glycol bis (succinimidyl succinate) to cross-link proteins and then subject to western blotting to assess the oligomeric status of VDAC1. Arrows indicate monomer and dimer forms of VDAC1. Asterisk indicates the intramolecular cross-linked bands. **c** PMHs pretreated with Fer-1 (1 μM) or VBIT-12 (15 μM or 20 μM) for 2 h were challenged with 20 mM APAP for 12 h. Cell viability was determined using CellTiter-Glo® luminescent cell viability assay (one-way ANOVA). **d** Representative images of calcein-AM, FerroOrange, Mito-FerroGreen, GSH, Bodipy 581/591 C11, DCFH-DA, MitoSOX, and JC-1 fluorescence in Hepa1-6 cells pretreated with Fer-1 (1 μM) or VBIT-12 (20 μM) for 2 h and then challenged with 20 mM APAP for 12 h. **e** Cell mito stress OCRs were measured using Seahorse XF analysis with the indicated reagents in PMHs pretreated with Fer-1 (1 μM) or VBIT-12 (20 μM) for 2 h and then challenged with 20 mM APAP for 6 h. The substrate was pyruvate. Arrows indicate the time when oligomycin, FCCP, and antimycin/rotenone were added to cells (n = 5–6/group, one-way ANOVA)

analysis (PLS-DA) demonstrated that the vehicle (control) and APAP groups (Supplementary Fig. 5a), UAMC3203 pretreatment and APAP groups (Supplementary Fig. 5b), and the VBIT-12 pretreatment and APAP groups (Supplementary Fig. 5c) could be separated. As illustrated in Supplementary Fig. 5d and Fig. 5e, levels of 241 lipid species significantly change following APAP challenge (fold-change > 1.5, P < 0.05) and revert back to normal in both UAMC3203- and VBIT-12-treated groups. Figure 6a presents Venn diagrams illustrating the 58 and 21 lipid species that were co-upregulated and downregulated, respectively, in both UAMC3203- and VBIT-12-pretreated groups compared with that of the APAP only group (fold-change > 1.5, P < 0.05). Volcano plots in Fig. 6b show that increased levels of CLs and CERs constituted the most profound changes following UAMC3203 or VBIT-12 pretreatment in APAP-injured liver tissues. Relative abundances of the 58 co-upregulated and 21 downregulated lipid species induced by UAMC3203 and VBIT-12 pretreatment are presented in Fig. 6c and d, respectively. In addition to drastic increases in levels of 7 CERs and 18 CLs consisting of various acyl chain lengths (C16-C26) and degrees of unsaturation, levels of 5 triglycerides consisting of long acyl chain lengths (C18-C28) were increased; however, levels of 11 different triglycerides consisting of shorter acyl chain lengths (C4-C10) were decreased in both the UAMC3203- and VBIT-12-treated groups compared with that in the APAP-only group. As triglyceride remodeling may also participate in the pathogenesis of AILI, it should be further investigated in the future. Furthermore, as CERs and CLs are important for mitochondrial structure and function, an increase in CER and CL content may mediate the protective effects of UAMC3203 or VBIT-12 on APAP-induced mitochondrial dysfunction and subsequent ferroptosis. In addition, the correlation of different lipids was explored (Supplementary Fig. 5f). Consistent with an increase in CER and CL content induced by UAMC3203 or VBIT-12 pretreatment, the ATP content of liver tissue in UAMC3203- or VBIT-12-pretreated groups was also significantly higher than that in the APAP only group (Fig. 6e). To further verify whether CER and CL mediate the protective effects of UAMC3203 or VBIT-12 on APAP-induced mitochondrial dysfunction and subsequent ferroptosis, we measured the mRNA levels of key genes responsible for CER and CL synthesis in liver tissues from mice challenged with APAP in the absence or presence of UAMC3203 or VBIT-12 pretreatment. The results showed that tafazzin (TAZ) was the CL-synthesizing enzyme that was most robustly induced by UAMC3203 or VBIT-12 (Fig. 6f). Meanwhile, SMPD1 was the CER-synthesizing enzyme that was most significantly upregulated by UAMC3203 or VBIT-12 (Fig. 6g).

Taken together, CER and CL levels were enhanced via UAMC3203 and VBIT-12, suggesting that changes in CER and CL content may participate in APAP-induced ferroptosis in hepatocytes.

Taz and *Smpd1*, responsible for CL and CER synthesis, affect APAP-induced mitochondrial dysfunction and subsequent ferroptosis in hepatocytes

As evidenced by the above results, TAZ and SMPD1 are the CL- and CER-synthesizing enzymes, respectively, that were most significantly upregulated by UAMC3203

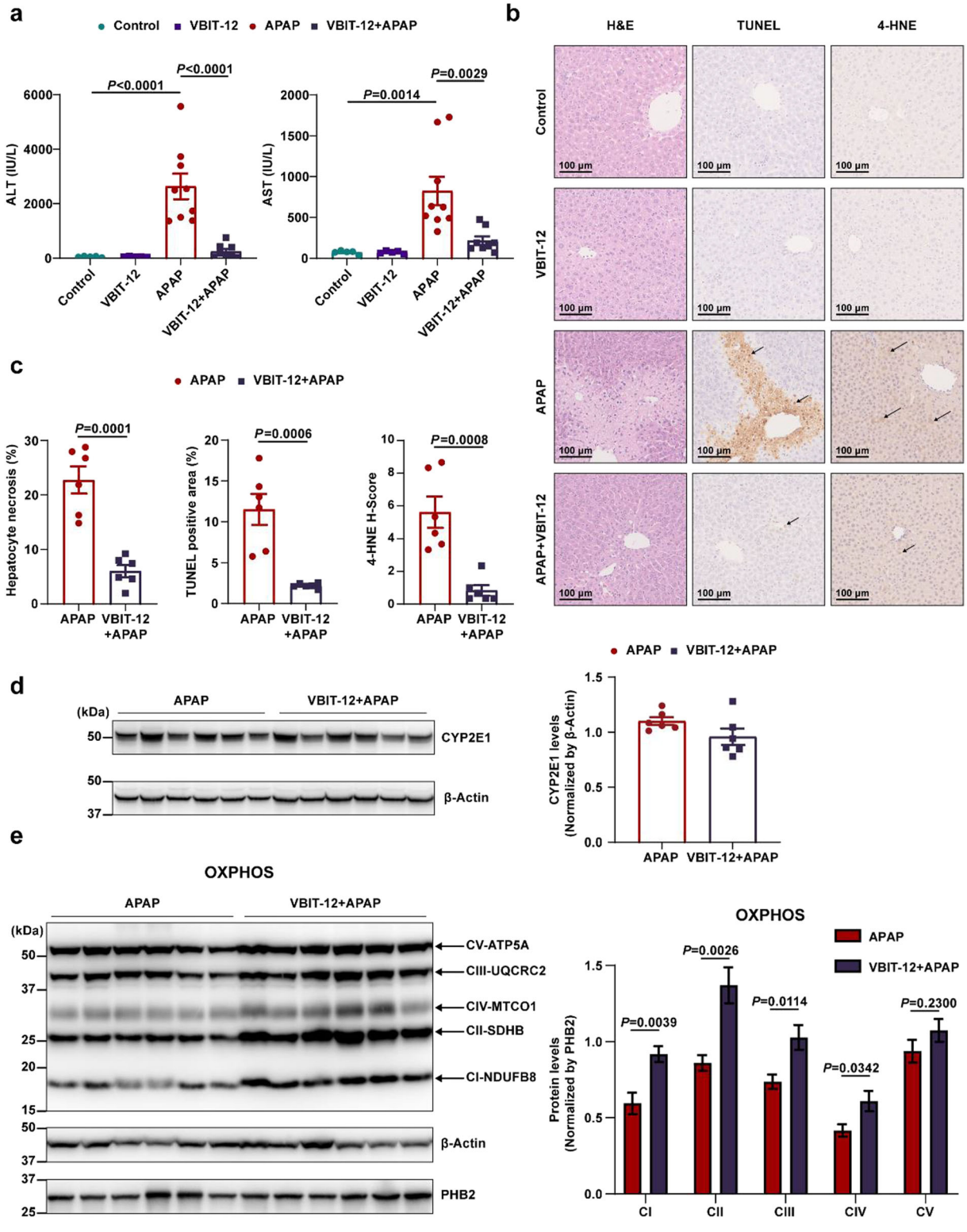
a
Control
VBIT-12
APAP
VBIT-12+APAP
P<0.0001
P<0.0001
ALT (IU/L)
6000
4000
2000
0
Control
VBIT-12
APAP
VBIT-12+APAP
P=0.0029
P=0.0014
AST (IU/L)
2000
1500
1000
500
0
Control
VBIT-12
APAP
VBIT-12+APAP
b
H&E
TUNEL
4-HNE
Control
VBIT-12
APAP
APAP+VBIT-12
100 μm
c
APAP
VBIT-12+APAP
P=0.0001
Hepatocyte necrosis (%)
30
20
10
0
APAP
VBIT-12 +APAP
P=0.0006
TUNEL positive area (%)
20
15
10
5
0
APAP
VBIT-12 +APAP
P=0.0008
4-HNE H-Score
10
8
6
4
2
0
APAP
VBIT-12 +APAP
d
(kDa)
APAP
VBIT-12+APAP
50
CYP2E1
50
37
β-Actin
APAP
VBIT-12+APAP
CYP2E1 levels (Normalized by β-Actin)
1.5
1.0
0.5
0.0
APAP
VBIT-12+APAP
e
OXPHOS
APAP
VBIT-12+APAP
(kDa)
50
37
25
20
15
CV-ATP5A
CIII-UQCRC2
CIV-MTCO1
CII-SDHB
CI-NDUFB8
50
37
β-Actin
37
25
PHB2
OXPHOS
APAP
VBIT-12+APAP
Protein levels (Normalized by PHB2)
1.5
1.0
0.5
0.0
P=0.0039
P=0.0026
P=0.0114
P=0.0342
P=0.2300
CI
CII
CIII
CIV
CV

Fig. 5 VBIT-12 protects mice against AILI and ferroptosis. Mice were pretreated with VBIT-12 (20 mg/kg) or vehicle via tail vein injection for 30 min prior to APAP (300 mg/kg) injection. After 10 h, serum and liver samples were collected. **a** Serum ALT and AST levels in vehicle- or VBIT-12-pretreated control or AILI mice were measured (n = 5–9 mice/group, t test). **b** Liver sections obtained from vehicle- or VBIT-12-pretreated AILI mice were stained with H&E, TUNEL, and 4-HNE immunohistochemical stains; scale bars represent 100 μm. Black arrows indicate positive staining. **c** Quantitative analyses of H&E, TUNEL, and 4-HNE stainings were performed (n = 6 mice/group, t test). **d** Western blot analysis of CYP2E1 protein levels in vehicle- or VBIT-12-pretreated AILI mice (n = 6 mice/group, t test). **e** Western blot analysis of OXPHOS complex protein levels and quantitative analyses of complex I-V in vehicle- or VBIT-12-pretreated AILI mice (n = 6 mice/group, t test). A mitochondrial protein PHB2 was used as a loading control

or VBIT-12 in AILI. To confirm whether *Taz* and *Smpd1* could affect AILI, we next used siRNA to reduce *Taz* or *Smpd1* expression in Hepa1-6 cells (Fig. 7a). Cell viability assays demonstrated aggravated cell death following the reduced expression of *Taz* or *Smpd1* in Hepa1-6 cells exposed to APAP overdose (Fig. 7b). Both basal and maximal OCRs in Hepa1-6 cells challenged with APAP overdose were decreased via *Taz* or *Smpd1* knockdown (Fig. 7c). Furthermore, when Hepa1-6 cells were challenged with APAP, lipid peroxidation was markedly increased by *Taz* or *Smpd1* siRNA compared with that by control siRNA (Fig. 7d). To further confirm these findings, we next investigated whether *Taz* overexpression could prevent APAP-induced hepatotoxicity. We transfected the *Taz* overexpression plasmid into Hepa1-6 cells to induce the *Taz* overexpression (Fig. 7e). Hepa1-6 cells overexpressing *Taz* showed increases in cell viability (Fig. 7f) and both basal and maximal mitochondrial OCRs (Fig. 7g) and decreases in lipid peroxidation (Fig. 7h) when challenged with APAP overdose compared with those of the control.

Together, knockdown of *Smpd1* and *Taz* expression responsible for CER and CL synthesis, respectively, aggravated APAP-induced mitochondrial dysfunction and ferroptosis in hepatocytes, whereas *Taz* overexpression protected against these processes.

Adduct levels of 4-HNE protein are increased in the liver samples of patients with DILI

4-HNE is the most abundant and reactive aldehyde product derived from the peroxidation of polyunsaturated fatty acids. It is regarded as a reliable indicator of endogenous lipid peroxidation in vivo (Podszun et al. 2020). To investigate ferroptosis and lipid peroxidation as the core feature of DILI in humans, we performed an immunohistochemistry assay to detect adduct levels of 4-HNE protein in liver biopsies. Staining and H-SCOREs were performed in needle biopsy liver samples from 34 patients with DILI and 48 patients with other liver diseases. In some patients, adduct levels of 4-HNE protein are detected in the cytoplasm; representative 4-HNE staining patterns from three patients of each group are shown in Fig. 8a. Patients with DILI had significantly higher adduct levels of 4-HNE protein than those in controls with AIH, CHB, and NAFLD (Fig. 8b). However, no difference in 4-HNE staining was present between patients with DILI and patients with ALD. DILI was classified as cholestatic ($R \leq 2$), mixed ($2 < R < 5$), or hepatocellular ($R \geq 5$) liver injury, as determined by the ratio (R) value and calculated as ([ALT/ULN]/[ALP/ULN]). The distribution of liver injury classification in patients with DILI is shown in Fig. 8c. According to Pearson correlation analysis for patients with hepatocellular DILI, the degree of 4-HNE adducts positivity correlated with ALT (r = 0.2068, P = 0.0440) (Fig. 8d), and did not correlate with AST or alkaline phosphatase (ALP) level (Supplementary Fig. 6a, b).

Taken together, adduct levels of 4-HNE protein were increased in the liver samples of patients with DILI compared with those of patients with AIH, CHB, and NAFLD.

Discussion

The present study demonstrated that ferroptosis was responsible for APAP-induced hepatocyte cell death in vivo and in vitro. Impaired energy generation, as caused by mitochondrial dysfunction associated with TCA cycle and fatty acid β-oxidation suppression, may drive APAP-induced ferroptosis. APAP overdose induced VDAC1 oligomerization in hepatocytes. Protecting mitochondria via VBIT-12, a VDAC1 oligomerization inhibitor, alleviated APAP-induced ferroptosis in vivo and in vitro. CER and CL levels were enhanced via a ferroptosis

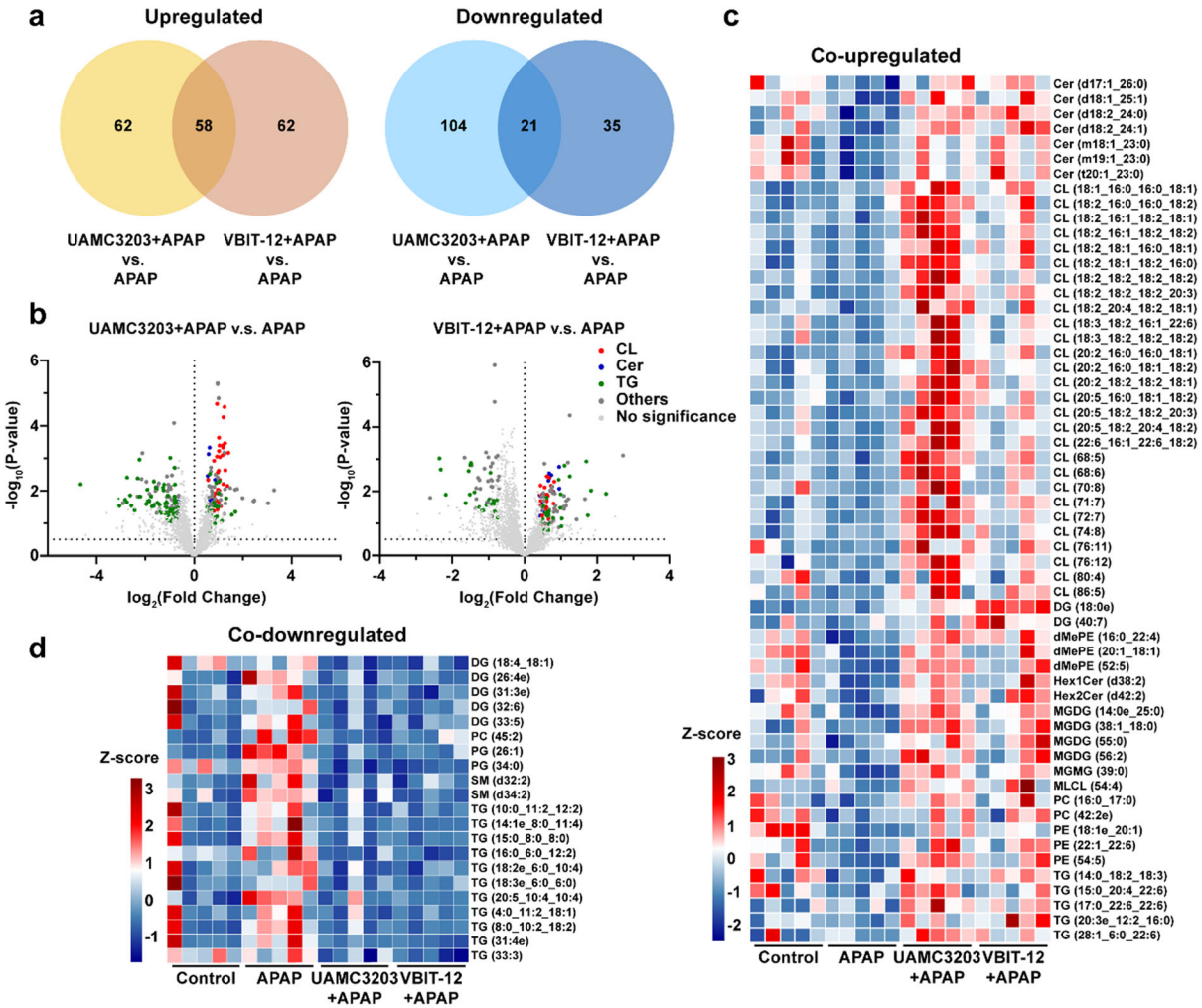
a
Upregulated
62
58
62
UAMC3203+APAP vs. APAP
VBIT-12+APAP vs. APAP
Downregulated
104
21
35
UAMC3203+APAP vs. APAP
VBIT-12+APAP vs. APAP
b
UAMC3203+APAP v.s. APAP
VBIT-12+APAP v.s. APAP
CL
Cer
TG
Others
No significance
-log10(P-value)
log2(Fold Change)
c
Co-upregulated
Cer (d17:1_26:0)
Cer (d18:1_25:1)
Cer (d18:2_24:0)
Cer (d18:2_24:1)
Cer (m18:1_23:0)
Cer (m19:1_23:0)
Cer (t20:1_23:0)
CL (18:1_16:0_16:0_18:1)
CL (18:2_16:0_16:0_18:2)
CL (18:2_16:1_18:2_18:1)
CL (18:2_16:1_18:2_18:2)
CL (18:2_18:1_16:0_18:1)
CL (18:2_18:1_18:2_16:0)
CL (18:2_18:2_18:2_18:2)
CL (18:2_18:2_18:2_20:3)
CL (18:2_20:4_18:2_18:1)
CL (18:3_18:2_16:1_22:6)
CL (18:3_18:2_18:2_18:2)
CL (20:2_16:0_16:0_18:1)
CL (20:2_16:0_18:1_18:2)
CL (20:2_18:2_18:2_18:1)
CL (20:5_16:0_18:1_18:2)
CL (20:5_18:2_18:2_20:3)
CL (20:5_18:2_20:4_18:2)
CL (22:6_16:1_22:6_18:2)
CL (68:5)
CL (68:6)
CL (70:8)
CL (71:7)
CL (72:7)
CL (74:8)
CL (76:11)
CL (76:12)
CL (80:4)
CL (86:5)
DG (18:0e)
DG (40:7)
dMePE (16:0_22:4)
dMePE (20:1_18:1)
dMePE (52:5)
Hex1Cer (d38:2)
Hex2Cer (d42:2)
MGDG (14:0e_25:0)
MGDG (38:1_18:0)
MGDG (55:0)
MGDG (56:2)
MGMG (39:0)
MLCL (54:4)
PC (16:0_17:0)
PC (42:2e)
PE (18:1e_20:1)
PE (22:1_22:6)
PE (54:5)
TG (14:0_18:2_18:3)
TG (15:0_20:4_22:6)
TG (17:0_22:6_22:6)
TG (20:3e_12:2_16:0)
TG (28:1_6:0_22:6)
Z-score
Control
APAP
UAMC3203 +APAP
VBIT-12 +APAP
d
Co-downregulated
DG (18:4_18:1)
DG (26:4e)
DG (31:3e)
DG (32:6)
DG (33:5)
PC (45:2)
PG (26:1)
PG (34:0)
SM (d32:2)
SM (d34:2)
TG (10:0_11:2_12:2)
TG (14:1e_8:0_11:4)
TG (15:0_8:0_8:0)
TG (16:0_6:0_12:2)
TG (18:2e_6:0_10:4)
TG (18:3e_6:0_6:0)
TG (20:5_10:4_10:4)
TG (4:0_11:2_18:1)
TG (8:0_10:2_18:2)
TG (31:4e)
TG (33:3)
Z-score
Control
APAP
UAMC3203 +APAP
VBIT-12 +APAP
e
APAP
UAMC3203+APAP
P=0.0320
ATP (μmol/g)
APAP
UAMC3203+APAP
APAP
VBIT-12+APAP
P=0.0180
ATP (μmol/g)
APAP
VBIT-12+APAP
f
APAP
UAMC3203+APAP
P=0.0016
n.s.
n.s.
Relative mRNA expression normalized by 36b4
Lclat1
Crls1
Taz
APAP
VBIT-12+APAP
P<0.0001
n.s.
n.s.
Relative mRNA expression normalized by Gapdh
Lclat1
Crls1
Taz
g
APAP
UAMC3203+APAP
P=0.0117
n.s.
P=0.0177
Relative mRNA expression normalized by 36b4
Degs1
Sgms1
Smpd1
APAP
VBIT-12+APAP
P=0.0074
n.s.
n.s.
Relative mRNA expression normalized by Gapdh
Degs1
Sgms1
Smpd1

Fig. 6 CER and CL levels are increased by UAMC3203 and VBIT-12. Mice were pretreated with UAMC3203 (10 mg/kg), VBIT-12 (20 mg/kg), or vehicle via tail vein injection for 30 min prior to APAP (300 mg/kg) injection. After 10 h, serum and liver samples were collected. **a** Venn diagrams depicting the number of significantly altered lipid species in the APAP-injured liver following UAMC3203 or VBIT-12 pretreatment (fold-change > 1.5, $P < 0.05$, $n = 5$ mice/group). **b** Volcano plots of significantly altered lipid species in the APAP-injured liver following UAMC3203 or VBIT-12 pretreatment (fold-change > 1.5, $P < 0.05$, $n = 5$ mice/group). **c** Heatmaps of significantly co-upregulated lipid species in the APAP-injured liver following UAMC3203 and VBIT-12 pretreatment (fold-change > 1.5, $P < 0.05$, $n = 5$ mice/group). **d** Heatmaps of significantly co-downregulated lipid species in the APAP-injured liver following UAMC3203 and VBIT-12 pretreatment (fold-change > 1.5, $P < 0.05$, $n = 5$ mice/group). **e** ATP content of liver tissue in APAP-injured mice pretreated with UAMC3203 or VBIT-12 ($n = 6$–7 mice/group, *t* test). **f** Relative mRNA levels of CL-synthesizing enzymes in Hepa1-6 cells challenged with 20 mM APAP for 12 h (one-way ANOVA). **g** Relative mRNA levels of CER-synthesizing enzymes in Hepa1-6 cells challenged with 20 mM APAP for 12 h (one-way ANOVA)

inhibitor and VBIT-12 in APAP-induced hepatocyte ferroptosis. Knockdown of *Smpd1* and *Taz*, which are responsible for CER and CL synthesis, respectively, aggravated APAP-induced mitochondrial dysfunction and ferroptosis in hepatocytes. Meanwhile, *Taz* overexpression could protect against AILI. In short, inhibiting VDAC1 oligomerization protected mitochondria and attenuated subsequent ferroptosis via increasing CER and CL levels in AILI. Adduct levels of lipid peroxidation indicator 4-HNE protein were increased in liver samples from patients with DILI, compared with those from patients with AIH, CHB, or NAFLD.

The protective role of DFO in AILI has been extensively in previous studies. Younes and Siegers showed that cultured hepatocytes pretreated with DFO were protected from APAP toxicity (Younes and Siegers 1985). Sakaida et al. reported that DFO partially protected against AILI in rats by reducing ALT level, mortality, and histopathological changes (Sakaida et al. 1995). Schnellmann et al. found that a single dose of DFO via intraperitoneal injection had no significant effect on APAP-induced hepatotoxicity, but repeated doses decreased the 12-h toxicity (Schnellmann et al. 1999). Yamada et al. reported that mice were intraperitoneally injected with DFO (100 mg/kg/day) for 7 consecutive days before APAP challenge. It was found that DFO treatment significantly inhibited APAP-induced hepatotoxicity (Yamada et al. 2020). Lorincz et al. reported that Fer-1 had a significant inhibitory effect on APAP-induced PMH death (Lorincz et al. 2015). Yamada et al. demonstrated the protective effect of Fer-1 on AILI in vivo. In the study, Fer-1 (10 mg/kg) was injected intraperitoneally 1 h prior to APAP administration (Yamada et al. 2020). Here, we did not use intraperitoneal injection; instead, we chose tail vein injection to administer DFO and UAMC3203, a compound with enhanced in vivo efficacy of Fer-1. The protective roles of DFO and UAMC3203 in AILI indicated that ferroptosis was responsible for APAP-induced hepatoxicity.

APAP-injured hepatocytes exhibit characteristic morphological changes in ferroptosis, including condensed mitochondrial membrane densities and a reduced volume, iron overload in mitochondria, accumulated mitochondrial ROS, and loss of MMP. How mitochondria acquire iron are not well understood. It has been proposed that extracellular iron can be directly delivered to the mitochondria and cytosolic iron can be taken up by mitochondria (Lange et al. 1999; Flatmark and Romslo 1975; Paul et al. 2017). Recently, Hu J et al. reported that APAP acted on lysosomes, which led to leakage of iron into the cytosol and its uptake by mitochondria (Hu and Lemasters 2020). Inhibition of mitochondrial fatty acid β-oxidation has been established as an important mechanism of APAP-induced hepatotoxicity (Chen et al. 2009; Yapar et al. 2007; Nowaczyk et al. 2000; Chen et al. 2000; Patterson et al. 2012). Promoting fatty acid β-oxidation might be a strategy to alleviate AILI. Our data also suggested that APAP overdose led to decreased basal and maximal mitochondrial OCRs and reduced fatty acid oxidation capacity in hepatocytes. Our targeted metabolomic data suggested that the levels of TCA cycle metabolites, drastically increased via Fer-1 in the presence of APAP challenge. This observation strongly implied that ATP insufficiency due to fatty acid β-oxidation and TCA cycle disruption in the mitochondria might play a central role in APAP-induced ferroptosis.

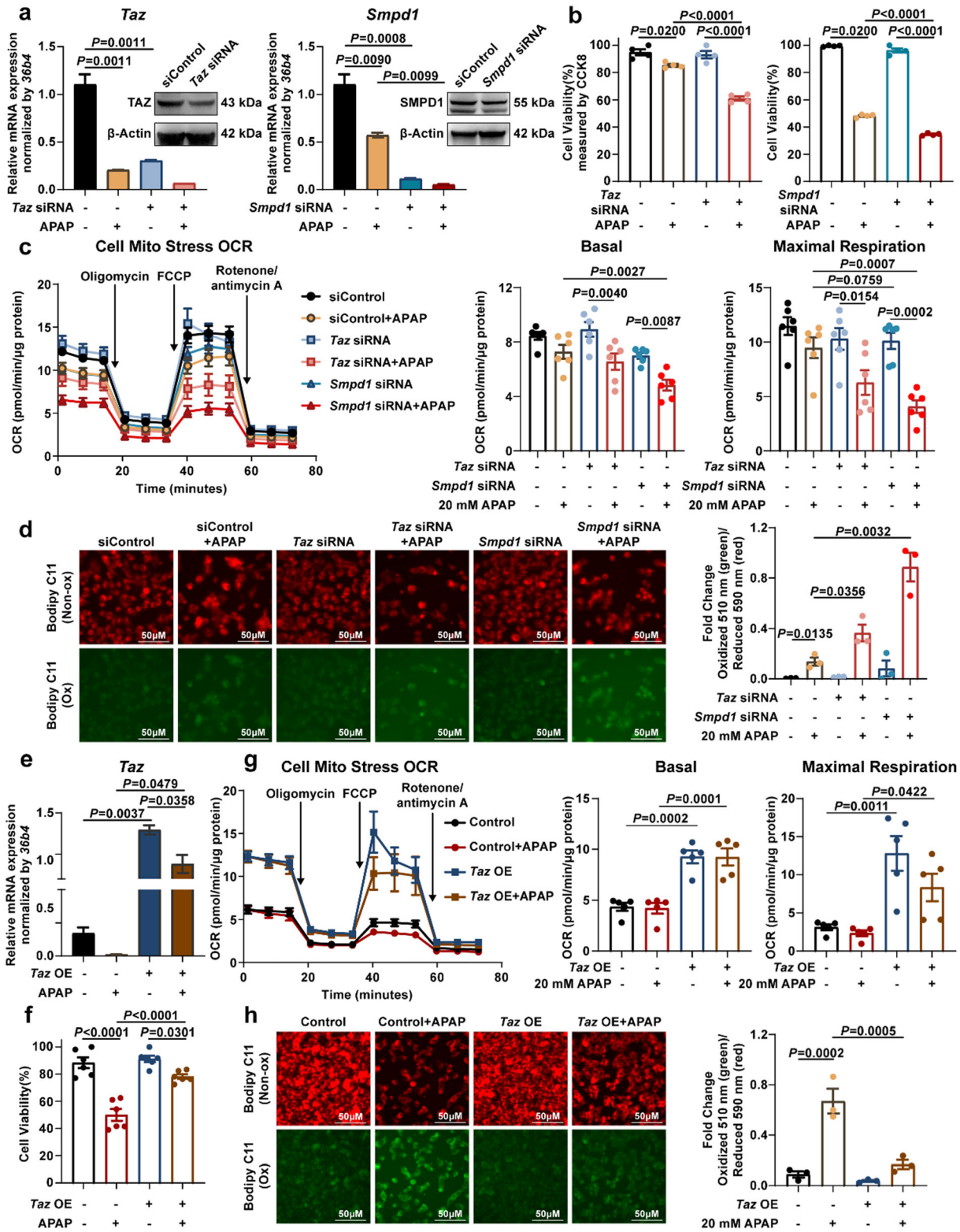
a
Taz
Smpd1
Relative mRNA expression normalized by 36b4
P=0.0011
P=0.0008
P=0.0090
P=0.0099
siControl
Taz siRNA
Smpd1 siRNA
TAZ
SMPD1
β-Actin
43 kDa
55 kDa
42 kDa
Taz siRNA
Smpd1 siRNA
APAP
b
Cell Viability(%) measured by CCK8
Cell Viability(%)
P<0.0001
P=0.0200
P<0.0001
c
Cell Mito Stress OCR
Oligomycin
FCCP
Rotenone/ antimycin A
OCR (pmol/min/μg protein)
Time (minutes)
siControl
siControl+APAP
Taz siRNA
Taz siRNA+APAP
Smpd1 siRNA
Smpd1 siRNA+APAP
Basal
Maximal Respiration
P=0.0027
P=0.0040
P=0.0087
P=0.0007
P=0.0759
P=0.0154
P=0.0002
20 mM APAP
d
siControl
siControl +APAP
Taz siRNA
Taz siRNA +APAP
Smpd1 siRNA
Smpd1 siRNA +APAP
Bodipy C11 (Non-ox)
Bodipy C11 (Ox)
50μM
Fold Change Oxidized 510 nm (green)/ Reduced 590 nm (red)
P=0.0032
P=0.0356
P=0.0135
e
Taz
Taz OE
P=0.0479
P=0.0358
P=0.0037
f
P<0.0001
P<0.0001
P=0.0301
g
Cell Mito Stress OCR
Control
Control+APAP
Taz OE
Taz OE+APAP
Basal
Maximal Respiration
P=0.0001
P=0.0002
P=0.0422
P=0.0011
h
Control
Control+APAP
Taz OE
Taz OE+APAP
P=0.0005
P=0.0002

Fig. 7 *Taz* and *Smpd1*, responsible for CL and CER synthesis, affect APAP-induced mitochondrial dysfunction and subsequent ferroptosis in hepatocytes. **a** Knockdown of *Taz* and *Smpd1* was confirmed by quantitative reverse transcription PCR and western blot analysis in Hepa1-6 cells treated with control, *Taz*, and *Smpd1* siRNA in the presence and absence of 20 mM APAP for 12 h (one-way ANOVA). **b** *Taz* and *Smpd1* knockdown Hepa1-6 cells were challenged with 20 mM APAP for 12 h. Cell viability was determined using a CellTiter-Glo® Luminescent Cell Viability Assay or CCK8 assay (one-way ANOVA). **c** Cell mito stress OCRs were measured using Seahorse XF analysis with the indicated reagents in *Taz* and *Smpd1* knockdown Hepa1-6 cells challenged with 20 mM APAP for 3 h. Arrows indicate the time when oligomycin, FCCP, and antimycin/rotenone were added to cells (n = 6/group, one-way ANOVA). **d** Hepa1-6 cells were subject to the same treatment as in (**a**); levels of lipid peroxidation were determined using BODIPY 581/591 C11 staining (t test). **e** Overexpression of *Taz* was confirmed by quantitative reverse transcription polymerase chain reaction in Hepa1-6 cells treated with control and *Taz* overexpression plasmid in the presence and absence of 20 mM APAP for 12 h (one-way ANOVA). **f** *Taz*-overexpressing Hepa1-6 cells were challenged with 20 mM APAP for 12 h. Cell viability was determined using a CellTiter-Glo® luminescent cell viability assay (one-way ANOVA). **g** Cell mito stress OCRs were measured using seahorse XF analysis with the indicated reagents in *Taz*-overexpressing Hepa1-6 cells challenged with 20 mM APAP for 6 h. Arrows indicate the time when oligomycin, FCCP, and antimycin/rotenone were added to cells (n = 6/group, one-way ANOVA). **h** Hepa1-6 cells were subject to the same treatment as in **e**; levels of lipid peroxidation were determined using BODIPY 581/591 C11 staining (t test)

More recently, the role of VDAC1 in ferroptosis has been investigated. VDAC has been shown as a potential target of the ferroptosis inducer erastin (Yagoda et al. 2007). Iron ions may enter the mitochondrial intermembrane space via VDAC in the MOM (Lange et al. 1999). Lipper et al. reported that [2Fe-2S] mitoNEET anchored in outer mitochondria could bind in the central cavity of VDAC, thereby regulating its gating redox dependently. Addition of the VDAC inhibitor 4,4′-diisothiocyanatostilbene-2,2′-disulfonate (DIDS) prevented mitoNEET-dependent iron accumulation in mitochondria (Lipper et al. 2019). In hippocampal HT22 cells, DIDS also significantly protected against glutamate-induced ferroptosis and mitochondrial fragmentation (Nagakannan et al. 2019). Liproxstatin-1, a ferroptosis inhibitor, protected the mouse myocardium against ischemia/reperfusion injury, which was mediated by a reduction in VDAC1 levels and oligomerization (Baba et al. 2018). In accordance with these previous reports, our data demonstrated that VDAC oligomerization was markedly induced by APAP in hepatocytes and that VBIT-12 dramatically attenuated mitochondria dysfunction and ferroptosis in vivo and in vitro.

Our lipidomic profiles suggested that relative amounts of CER and CL in the liver tissues of VBIT-12- or UAMC3203-treated APAP-injured mice markedly increased compared to those of APAP-injured mice. CERs act locally in mitochondria, regulating mitochondrial apoptosis and/or mitophagy. CER is generated via the de novo CER synthesis, sphingomyelinase, and salvage pathways (Jenkins et al. 2010; Hernandez-Corbacho et al. 2017). Our results showed that acid sphingomyelinase (ASMase, *Smpd1*) was the CER synthesis gene that was most significantly upregulated by UAMC3203 and VBIT-12. SMPD1 localizes within the endolysosomal compartment, catalyzing the cleavage of sphingomyelin to CER. *Smpd1*$^{-/-}$ mice exhibited higher mortality following APAP overdose than their *Smpd1*$^{+/+}$ littermates. *Smpd1*$^{-/-}$ hepatocytes displayed aggravated APAP-induced cell death and defective mitochondrial quality control (Baulies et al. 2015). CLs, located in the inner mitochondrial membrane, are critical for inner membrane integrity and the preservation of mitochondrial oxidative phosphorylation (Ren et al. 2014). APAP remodeled fatty acid composition of CL from tetralinoleoyl to linoleoyltrioleoyl-CL, which is involved in decreased mitochondrial respiration (Vergeade et al. 2016). Our data demonstrated that *Taz* was the CL synthesis gene that was most significantly upregulated by UAMC3203 and VBIT-12. TAZ is an enzyme responsible for the remodeling of immature CL, by exchanging acyl groups between CL and other phospholipids (Szczepanek et al. 2016). In humans, mutations in the *Taz* gene result in CL remodeling, potentially leading to Barth syndrome. In mice, *Taz* knockdown caused an increased monolysocardiolipin:CL ratio, cardiomyopathy, prenatal-perinatal lethality, damaged mitochondria, and decreased respiratory activity (Ren et al. 2014). In accordance with the above reports, we found that *Smpd1* and *Taz* knockdown

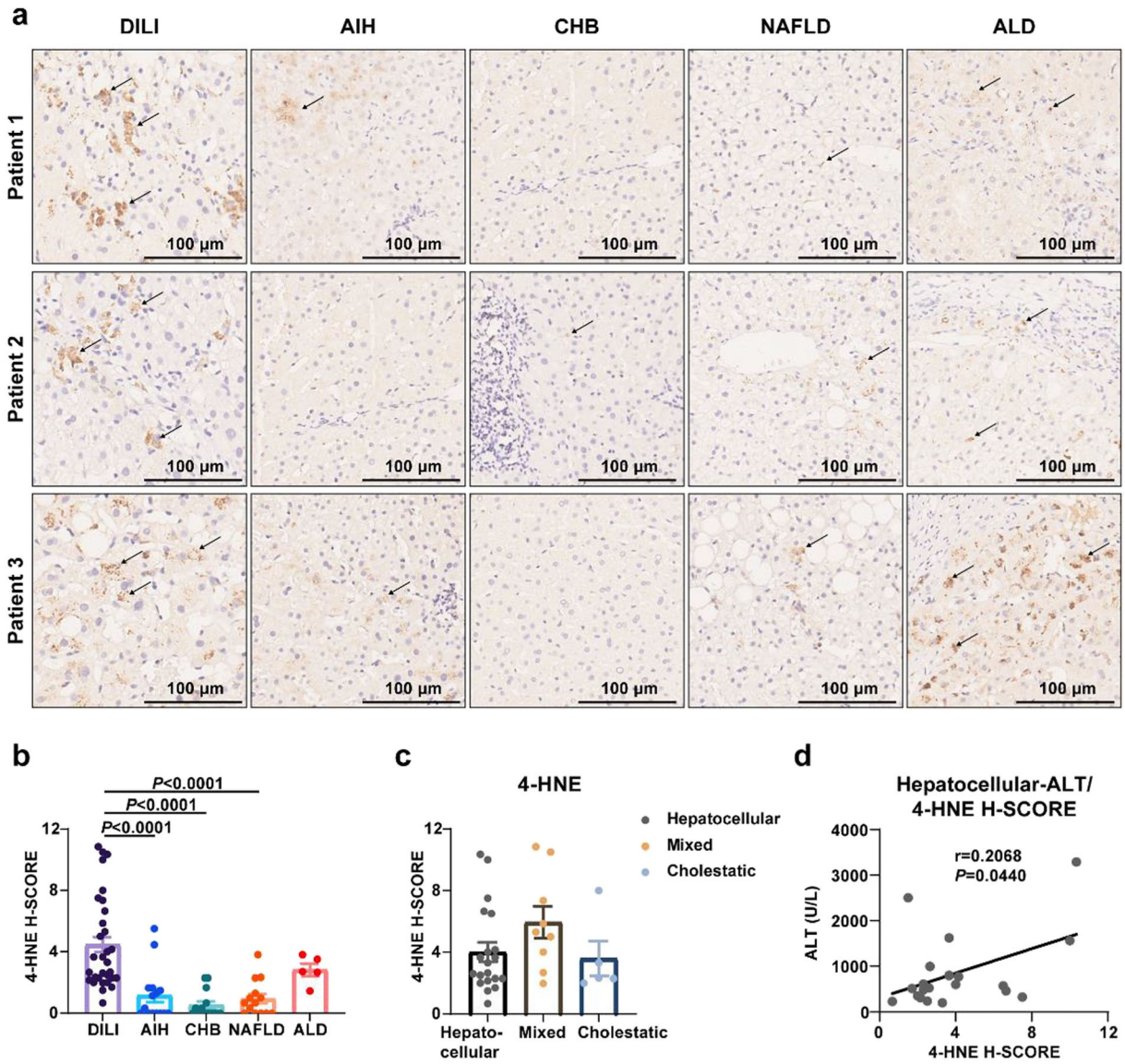

Fig. 8 Adduct levels of 4-HNE protein are increased in the liver samples of patients with DILI. **a** Representative 4-HNE staining patterns in liver samples from three patients with DILI and other liver diseases; scale bars represent 100 μm. Black arrows indicate positive staining. **b** The H-SCOREs of 4-HNE in liver samples obtained from 34 patients with DILI and 48 patients with other liver diseases (15 autoimmune liver disease, 14 chronic viral hepatitis B, 14 non-alcoholic fatty liver disease steatosis, and 5 alcoholic liver disease patients) (one-way ANOVA). **c** Distribution of liver injury classifications and corresponding 4-HNE H-SCOREs in patients with DILI (one-way ANOVA). **d** Pearson correlation was performed between serum ALT levels in 20 patients with hepatocellular DILI and H-SCOREs of 4-HNE staining

aggravated APAP-induced mitochondrial dysfunction and ferroptosis. Furthermore, we observed that *Taz* overexpression could protect against AILI. These findings suggest that protecting mitochondria via *Smpd1* and *Taz* manipulation to maintain CER and CL content might be an essential therapeutic strategy for AILI and even potentially DILI. However, the molecular mechanism by which VDAC inhibition promotes the transcriptional expression of *Taz* and *Smpd1* is not quite clear. This is a limitation of our present study and requires further investigation in the future.

4-HNE, derived from the peroxidation of polyunsaturated fatty acids, can reveal endogenous lipid peroxidation and ferroptosis. Liver biopsies from patients with NAFLD showed higher adduct levels of 4-HNE protein, compared to controls (Podszun et al. 2020). 4-HNE staining significantly enhanced in the hepatocytes of patients with ALD and was completely absent in normal human liver (Hayashi et al. 2013). Our data suggested that adduct levels of 4-HNE protein specifically increased in the liver samples of patients with DILI and ALD than those of patients with other common liver diseases. Drugs and alcohol impair liver functions through similar mechanisms, including CYP2E1 induction, GSH depletion, and the enhancement of oxidative stress.

More recently, peroxynitrite emerged as a critical mediator of mitochondrial damage in AILI. MnSOD (SOD2) effectively prevents peroxynitrite formation and alleviates AILI (Jaeschke et al. 2021). However, MnSOD accelerates the formation of hydrogen peroxide, which together with iron can lead to lipid peroxidation. The effective protection of MnSOD was believed as an indication of the lack of biological relevance of lipid peroxidation in APAP-induced liver injury. Both SOD mimetics (Mito-tempo) and partial deficiency of the mitochondrial MnSOD that were utilized in previous reports were not part of the physiological regulation of SOD in APAP-induced hepatoxicity (Du et al. 2019; Du et al. 2017; Ramachandran et al. 2011). Based on our RNA-seq data and q-PCR validation in another cohort of mice (data not shown), SOD2 mRNA levels in mice liver were not upregulated upon APAP challenge. In the APAP-injured liver, whether the endogenous defense system mediated by SOD has toxicity needs to be further elucidated.

Overall, the current study provides conclusive evidence for the substantial involvement of VDAC1 oligomerization and mitochondrial damage in APAP-induced ferroptosis.

Supplementary Information The online version contains supplementary material available at https://doi.org/10.1007/s10565-021-09624-x.

Availability of data and material Data and materials used and/or analyzed during the current study are available from the corresponding authors on reasonable request.

Code availability Not applicable.

Author contributions B.N performed mouse and cell experiments and implemented the data analysis. Q.X and XH.L performed clinical evaluation and collected clinical samples. XH. L, Y.J, D.X, L.M, and J.L helped collecting samples andperformed western blot analysis and quantitative real-time PCR analysis. X.Z assisted with pathology and scoring. Y.Z. helped with bioinformatics analysis. XB.L, Y. Mao, and X.Z conceived and supervised the project and analyzed the data. XB.L. and B.N. wrote the manuscript. Prof. Sun Ning helped with manuscript reviewing and editing. All authors discussed the results and revised the manuscript.

Funding This work was supported by the National Natural Science Foundation of China (NSFC 31771308, NSFC 81970513, and NSFC 81670524), the Shanghai Municipal Natural Science Foundation (17ZR1401800), the Innovative Research Team of High-level Local Universities in Shanghai, Shanghai Key Laboratory of Bioactive Small Molecules (ZDSYS14005), the Major Project of National Thirteenth Five Plan (2017ZX09304016), the Project of Shanghai Shenkang Hospital Development Center (16CR2009A), and the Project of Clinical Research Center, Shanghai Jiao Tong University School of Medicine (DLY201607).

Declarations

Ethics approval All animal experiments were approved by the Animal Ethics Committee of Fudan University School of Basic Medical Sciences. Animal research was conducted in accordance with international guidelines. The clinical research was approved by the Ethics Committee of Shanghai Jiaotong University Renji Hospital in accordance with the ethical guidelines of the 1975 Declaration of Helsinki.

Consent to participate Not applicable.

Consent for publication Not applicable.

Conflict of interest The authors declare no competing interests.

References

Andrade RJ, Chalasani N, Bjornsson ES, Suzuki A, Kullak-Ublick GA, Watkins PB, et al. Drug-induced liver injury. Nat Rev Dis Primers. 2019;5(1):58. https://doi.org/10.1038/s41572-019-0105-0.

Baba Y, Higa JK, Shimada BK, Horiuchi KM, Suhara T, Kobayashi M, Woo JD, Aoyagi H, Marh KS, Kitaoka H, Matsui T. Protective effects of the mechanistic target of rapamycin against excess iron and ferroptosis in cardiomyocytes. Am J Physiol Heart Circ Physiol. 2018;314(3):H659–H68. https://doi.org/10.1152/ajpheart.00452.2017.

Baulies A, Ribas V, Nunez S, Torres S, Alarcon-Vila C, Martinez L, et al. Lysosomal cholesterol accumulation sensitizes to acetaminophen hepatotoxicity by impairing mitophagy. Sci Rep. 2015;5:18017. https://doi.org/10.1038/srep18017.

Ben-Hail D, Begas-Shvartz R, Shalev M, Shteinfer-Kuzmine A, Gruzman A, Reina S, de Pinto V, Shoshan-Barmatz V. Novel compounds targeting the mitochondrial protein vdac1 inhibit apoptosis and protect against mitochondrial dysfunction. J Biol Chem. 2016;291(48):24986–5003. https://doi.org/10.1074/jbc.M116.744284.

Bjornsson ES, Bergmann OM, Bjornsson HK, Kvaran RB, Olafsson S. Incidence, presentation, and outcomes in patients with drug-induced liver injury in the general population of iceland. Gastroenterology. 2013;144(7):1419–25, 25 e1-3; quiz e19-20. https://doi.org/10.1053/j.gastro.2013.02.006.

Bock FJ, Tait SWG. Mitochondria as multifaceted regulators of cell death. Nat Rev Mol Cell Biol. 2020;21(2):85–100. https://doi.org/10.1038/s41580-019-0173-8.

Chen C, Hennig GE, Whiteley HE, Corton JC, Manautou JE. Peroxisome proliferator-activated receptor alpha-null mice lack resistance to acetaminophen hepatotoxicity following clofibrate exposure. Toxicol Sci. 2000;57(2):338–44. https://doi.org/10.1093/toxsci/57.2.338.

Chen C, Krausz KW, Shah YM, Idle JR, Gonzalez FJ. Serum metabolomics reveals irreversible inhibition of fatty acid beta-oxidation through the suppression of pparalpha activation as a contributing mechanism of acetaminophen-induced hepatotoxicity. Chem Res Toxicol. 2009;22(4):699–707. https://doi.org/10.1021/tx800464q.

Church RJ, Kullak-Ublick GA, Aubrecht J, Bonkovsky HL, Chalasani N, Fontana RJ, Goepfert JC, Hackman F, King NMP, Kirby S, Kirby P, Marcinak J, Ormarsdottir S, Schomaker SJ, Schuppe-Koistinen I, Wolenski F, Arber N, Merz M, Sauer JM, et al. Candidate biomarkers for the diagnosis and prognosis of drug-induced liver injury: An international collaborative effort. Hepatology. 2019;69(2):760–73. https://doi.org/10.1002/hep.29802.

Devisscher L, Van Coillie S, Hofmans S, Van Rompaey D, Goossens K, Meul E, et al. Discovery of novel, drug-like ferroptosis inhibitors with in vivo efficacy. J Med Chem. 2018;61(22):10126–40. https://doi.org/10.1021/acs.jmedchem.8b01299.

Du K, Farhood A, Jaeschke H. Mitochondria-targeted antioxidant mito-tempo protects against acetaminophen hepatotoxicity. Arch Toxicol. 2017;91(2):761–73. https://doi.org/10.1007/s00204-016-1692-0.

Du K, Ramachandran A, Weemhoff JL, Woolbright BL, Jaeschke AH, Chao X, et al. Mito-tempo protects against acute liver injury but induces limited secondary apoptosis during the late phase of acetaminophen hepatotoxicity. Arch Toxicol. 2019;93(1):163–78. https://doi.org/10.1007/s00204-018-2331-8.

Ettel M, Gonzalez GA, Gera S, Eze O, Sigal S, Park JS, Xu R. Frequency and pathological characteristics of drug-induced liver injury in a tertiary medical center. Hum Pathol. 2017;68:92–8. https://doi.org/10.1016/j.humpath.2017.08.029.

European Association for the Study of the Liver. Electronic address eee, Clinical Practice Guideline Panel C, Panel m, representative EGB. Easl clinical practice guidelines: drug-induced liver injury. J Hepatol. 2019;70(6):1222–61. https://doi.org/10.1016/j.jhep.2019.02.014.

Flatmark T, Romslo I. Energy-dependent accumulation of iron by isolated rat liver mitochondria. Requirement of reducing equivalents and evidence for a unidirectional flux of fe(ii) across the inner membrane. J Biol Chem. 1975;250(16):6433–8.

Hassan A, Fontana RJ. The diagnosis and management of idiosyncratic drug-induced liver injury. Liver Int. 2019;39(1):31–41. https://doi.org/10.1111/liv.13931.

Hayashi N, George J, Takeuchi M, Fukumura A, Toshikuni N, Arisawa T, Tsutsumi M. Acetaldehyde-derived advanced glycation end-products promote alcoholic liver disease. PLoS One. 2013;8(7):e70034. https://doi.org/10.1371/journal.pone.0070034.

Hernandez-Corbacho MJ, Salama MF, Canals D, Senkal CE, Obeid LM. Sphingolipids in mitochondria. Biochim Biophys Acta Mol Cell Biol Lipids. 2017;1862(1):56–68. https://doi.org/10.1016/j.bbalip.2016.09.019.

Hong W, Guo F, Yang M, Xu D, Zhuang Z, Niu B, Bai Q, Li X. Hydroxysteroid sulfotransferase 2b1 affects gastric epithelial function and carcinogenesis induced by a carcinogenic agent. Lipids Health Dis. 2019;18(1):203. https://doi.org/10.1186/s12944-019-1149-6.

Hu J, Lemasters JJ. Suppression of iron mobilization from lysosomes to mitochondria attenuates liver injury after acetaminophen overdose in vivo in mice: protection by minocycline. Toxicol Appl Pharmacol. 2020;392:114930. https://doi.org/10.1016/j.taap.2020.114930.

Jaeschke H. Mitochondrial dysfunction as a mechanism of drug-induced hepatotoxicity: current understanding and future perspectives. Journal of Clinical and Translational Research. 2018;4(1):75–100. https://doi.org/10.18053/jctres.04.201801.005.

Jaeschke H, Xie Y, McGill MR. Acetaminophen-induced liver injury: from animal models to humans. J Clin Transl Hepatol. 2014;2(3):153–61. https://doi.org/10.14218/JCTH.2014.00014.

Jaeschke H, Adelusi OB, Ramachandran A. Ferroptosis and acetaminophen hepatotoxicity - are we going down another rabbit hole? Gene Expr. 2021;20:169–78. https://doi.org/10.3727/105221621x16104581979144.

Jenkins RW, Canals D, Idkowiak-Baldys J, Simbari F, Roddy P, Perry DM, Kitatani K, Luberto C, Hannun YA. Regulated secretion of acid sphingomyelinase: implications for selectivity of ceramide formation. J Biol Chem. 2010;285(46):35706–18. https://doi.org/10.1074/jbc.M110.125609.

Jollow DJ, Mitchell JR, Potter WZ, Davis DC, Gillette JR, Brodie BB. Acetaminophen-induced hepatic necrosis .2. Role of covalent binding in-vivo. J Pharmacol Exp Ther. 1973;187(1):195–202.

Kim J, Gupta R, Blanco LP, Yang S, Shteinfer-Kuzmine A, Wang K, Zhu J, Yoon HE, Wang X, Kerkhofs M, Kang H, Brown AL, Park SJ, Xu X, Zandee van Rilland E, Kim MK, Cohen JI, Kaplan MJ, Shoshan-Barmatz V, Chung JH. Vdac oligomers form mitochondrial pores to release mtdna fragments and promote lupus-like disease. Science. 2019;366(6472):1531–6. https://doi.org/10.1126/science.aav4011.

Kullak-Ublick GA, Andrade RJ, Merz M, End P, Benesic A, Gerbes AL, Aithal GP. Drug-induced liver injury: recent advances in diagnosis and risk assessment. Gut. 2017;66(6):1154–64. https://doi.org/10.1136/gutjnl-2016-313369.

Lange H, Kispal G, Lill R. Mechanism of iron transport to the site of heme synthesis inside yeast mitochondria. J Biol Chem. 1999;274(27):18989–96. https://doi.org/10.1074/jbc.274.27.18989.

Lewis JH. Diagnosis: liver biopsy differentiates dili from autoimmune hepatitis. Nat Rev Gastroenterol Hepatol. 2011;8(10):540–2. https://doi.org/10.1038/nrgastro.2011.140.

Li C, Ming Y, Hong W, Tang Y, Lei X, Li X, Mao Y. Comparison of hepatic transcriptome profiling between acute liver injury and acute liver failure induced by acetaminophen in mice. Toxicol Lett. 2018;283:69–76. https://doi.org/10.1016/j.toxlet.2017.11.020.

Lipper CH, Stofleth JT, Bai F, Sohn YS, Roy S, Mittler R, Nechushtai R, Onuchic JN, Jennings PA. Redox-dependent gating of vdac by mitoneet. Proc Natl Acad Sci U S A. 2019;116(40):19924–9. https://doi.org/10.1073/pnas.1908271116.

Lorincz T, Jemnitz K, Kardon T, Mandl J, Szarka A. Ferroptosis is involved in acetaminophen induced cell death. Pathol Oncol Res. 2015;21(4):1115–21. https://doi.org/10.1007/s12253-015-9946-3.

Nagakannan P, Islam MI, Karimi-Abdolrezaee S, Eftekharpour E. Inhibition of vdac1 protects against glutamate-induced oxytosis and mitochondrial fragmentation in hippocampal ht22 cells. Cell Mol Neurobiol. 2019;39(1):73–85. https://doi.org/10.1007/s10571-018-0634-1.

Nowaczyk MJ, Whelan D, Hill RE, Clarke JT, Pollitt RJ. Long-chain hydroxydicarboxylic aciduria, carnitine depletion and acetaminophen exposure. J Inherit Metab Dis. 2000;23(2):188–9. https://doi.org/10.1023/a:1005630218986.

Patterson AD, Shah YM, Matsubara T, Krausz KW, Gonzalez FJ. Peroxisome proliferator-activated receptor alpha induction of uncoupling protein 2 protects against acetaminophen-induced liver toxicity. Hepatology. 2012;56(1):281–90. https://doi.org/10.1002/hep.25645.

Paul BT, Manz DH, Torti FM, Torti SV. Mitochondria and iron: Current questions. Expert Rev Hematol. 2017;10(1):65–79. https://doi.org/10.1080/17474086.2016.1268047.

Podszun MC, Chung JY, Ylaya K, Kleiner DE, Hewitt SM, Rotman Y. 4-hne immunohistochemistry and image analysis for detection of lipid peroxidation in human liver samples using vitamin e treatment in nafld as a proof of concept. J Histochem Cytochem. 2020;68(9):635–43. https://doi.org/10.1369/0022155420946402.

Ramachandran A, Jaeschke H. Acetaminophen hepatotoxicity: a mitochondrial perspective. Adv Pharmacol. 2019;85:195–219. https://doi.org/10.1016/bs.apha.2019.01.007.

Ramachandran A, Lebofsky M, Weinman SA, Jaeschke H. The impact of partial manganese superoxide dismutase (sod2)-deficiency on mitochondrial oxidant stress, DNA fragmentation and liver injury during acetaminophen hepatotoxicity. Toxicol Appl Pharmacol. 2011;251(3):226–33. https://doi.org/10.1016/j.taap.2011.01.004.

Ren M, Phoon CKL, Schlame M. Metabolism and function of mitochondrial cardiolipin. Prog Lipid Res. 2014;55:1–16. https://doi.org/10.1016/j.plipres.2014.04.001.

Sakaida I, Kayano K, Wasaki S, Nagatomi A, Matsumura Y, Okita K. Protection against acetaminophen-induced liver injury in vivo by an iron chelator, deferoxamine. Scand J Gastroenterol. 1995;30(1):61–7. https://doi.org/10.3109/00365529509093237.

Schnellmann JG, Pumford NR, Kusewitt DF, Bucci TJ, Hinson JA. Deferoxamine delays the development of the hepatotoxicity of acetaminophen in mice. Toxicol Lett. 1999;106(1):79–88. https://doi.org/10.1016/s0378-4274(99)00021-1.

Sgro C, Clinard F, Ouazir K, Chanay H, Allard C, Guilleminet C, Lenoir C, Lemoine A, Hillon P. Incidence of drug-induced hepatic injuries: a French population-based study. Hepatology. 2002;36(2):451–5. https://doi.org/10.1053/jhep.2002.34857.

Shen T, Liu Y, Shang J, Xie Q, Li J, Yan M, Xu J, Niu J, Liu J, Watkins PB, Aithal GP, Andrade RJ, Dou X, Yao L, Lv F, Wang Q, Li Y, Zhou X, Zhang Y, et al. Incidence and etiology of drug-induced liver injury in mainland china. Gastroenterology. 2019;156(8):2230–41 e11. https://doi.org/10.1053/j.gastro.2019.02.002.

Shoshan-Barmatz V, Nahon-Crystal E, Shteinfer-Kuzmine A, Gupta R. Vdac1, mitochondrial dysfunction, and alzheimer's disease. Pharmacol Res. 2018;131:87–101. https://doi.org/10.1016/j.phrs.2018.03.010.

Stockwell BR, Friedmann Angeli JP, Bayir H, Bush AI, Conrad M, Dixon SJ, Fulda S, Gascón S, Hatzios SK, Kagan VE, Noel K, Jiang X, Linkermann A, Murphy ME, Overholtzer M, Oyagi A, Pagnussat GC, Park J, Ran Q, et al. Ferroptosis: a regulated cell death nexus linking metabolism, redox biology, and disease. Cell. 2017;171(2):273–85. https://doi.org/10.1016/j.cell.2017.09.021.

Szczepanek K, Allegood J, Aluri H, Hu Y, Chen Q, Lesnefsky EJ. Acquired deficiency of tafazzin in the adult heart: Impact on mitochondrial function and response to cardiac injury. Biochim Biophys Acta. 2016;1861(4):294–300. https://doi.org/10.1016/j.bbalip.2015.12.004.

Tujios S, Fontana RJ. Mechanisms of drug-induced liver injury: from bedside to bench. Nat Rev Gastroenterol Hepatol. 2011;8(4):202–11. https://doi.org/10.1038/nrgastro.2011.22.

Vergeade A, Bertram CC, Bikineyeva AT, Zackert WE, Zinkel SS, May JM, Dikalov SI, Roberts LJ II, Boutaud O. Cardiolipin fatty acid remodeling regulates mitochondrial function by modifying the electron entry point in the respiratory chain. Mitochondrion. 2016;28:88–95. https://doi.org/10.1016/j.mito.2016.04.002.

Wang Z, Yang X, Chen L, Zhi X, Lu H, Ning Y, Yeong J, Chen S, Yin L, Wang X, Li X. Upregulation of hydroxysteroid sulfotransferase 2b1b promotes hepatic oval cell proliferation by modulating oxysterol-induced lxr activation in a mouse model of liver injury. Arch Toxicol. 2017;91(1):271–87. https://doi.org/10.1007/s00204-016-1693-z.

Wang H, Liu C, Zhao Y, Gao G. Mitochondria regulation in ferroptosis. Eur J Cell Biol. 2020;99(1):151058. https://doi.org/10.1016/j.ejcb.2019.151058.

Wu H, Wang F, Ta N, Zhang T, Gao W. The multifaceted regulation of mitochondria in ferroptosis. Life (Basel, Switzerland). 2021;11(3):222. https://doi.org/10.3390/life11030222.

Yagoda N, von Rechenberg M, Zaganjor E, Bauer AJ, Yang WS, Fridman DJ, Wolpaw AJ, Smukste I, Peltier JM, Boniface JJ, Smith R, Lessnick SL, Sahasrabudhe S, Stockwell BR. Ras-raf-mek-dependent oxidative cell death involving voltage-dependent anion channels. Nature. 2007;447(7146):864–8. https://doi.org/10.1038/nature05859.

Yamada N, Karasawa T, Kimura H, Watanabe S, Komada T, Kamata R, Sampilvanjil A, Ito J, Nakagawa K, Kuwata H,

Hara S, Mizuta K, Sakuma Y, Sata N, Takahashi M. Ferroptosis driven by radical oxidation of n-6 polyunsaturated fatty acids mediates acetaminophen-induced acute liver failure. Cell Death Dis. 2020;11(2):144. https://doi.org/10.1038/s41419-020-2334-2.

Yapar K, Kart A, Karapehlivan M, Atakisi O, Tunca R, Erginsoy S, Citil M. Hepatoprotective effect of l-carnitine against acute acetaminophen toxicity in mice. Exp Toxicol Pathol. 2007;59(2):121–8. https://doi.org/10.1016/j.etp.2007.02.009.

Younes M, Siegers CP. The role of iron in the paracetamol- and ccl4-induced lipid peroxidation and hepatotoxicity. Chem Biol Interact. 1985;55(3):327–34. https://doi.org/10.1016/s0009-2797(85)80139-3.

Yu YC, Mao YM, Chen CW, Chen JJ, Chen J, Cong WM, et al. Csh guidelines for the diagnosis and treatment of drug-induced liver injury. Hepatol Int. 2017;11(3):221–41. https://doi.org/10.1007/s12072-017-9793-2.